Predictive modeling of CO_2 sequestration in deep saline sandstone reservoirs: Impacts of geochemical kinetics

Victor N. Balashov[1], George D. Guthrie[2], J. Alexandra Hakala[2], Christina L. Lopano[2], J. Donald Rimstidt[3], Susan L. Brantley[1]

[1]Earth and Environmental Systems Institute, 2217 EES Building, Pennsylvania State University, University Park, PA 16802; [2] U.S. Department of Energy, National Energy and Technology Laboratory, 626 Cochrans Mill Road, Pittsburgh, PA 15236; [3]Department of Geosciences, Virginia Polytechnic Institute and State University, Blacksburg, VA 24061

Abstract

One idea for mitigating the increase in fossil-fuel generated CO_2 in the atmosphere is to inject CO_2 into subsurface saline sandstone reservoirs. To decide whether to try such sequestration at a globally significant scale will require the ability to predict the fate of injected CO_2. Thus, models are needed to predict the rates and extents of subsurface rock-water-gas interactions. Several reactive transport models for CO_2 sequestration created in the last decade predicted sequestration in sandstone reservoirs of ~17 to ~90 kg CO_2 m^{-3}. To build confidence in such models, a baseline problem including rock + water chemistry is proposed as the basis for future modeling so that both the models and the parameterizations can be compared systematically. In addition, a reactive diffusion model is used to investigate the fate of injected supercritical CO_2 fluid in the proposed baseline reservoir + brine system. In the baseline problem, injected CO_2 is redistributed from the supercritical (SC) free phase by dissolution into pore brine and by formation of carbonates in the sandstone. The numerical transport model incorporates a full kinetic description of mineral-water reactions under the assumption that transport is by diffusion only. Sensitivity tests were also run to understand which mineral kinetics reactions are important for CO_2 trapping.

The diffusion transport model shows that for the first ~20 years after CO_2 diffusion initiates, CO_2 is mostly consumed by dissolution into the brine to form $CO_{2,aq}$ (solubility trapping). From 20-200 years, both solubility and mineral trapping are important as calcite precipitation is driven by dissolution of oligoclase. From 200 to 1000 years, mineral trapping is the most important sequestration mechanism, as smectite dissolves and calcite precipitates. Beyond 2000 years, most trapping is due to formation of aqueous HCO_3^-. Ninety-seven percent of the maximum CO_2 sequestration, 34.5 kg CO_2 per m^3 of sandstone, is attained by 4000 years even though the system does not achieve chemical equilibrium until ~25,000 years. This maximum represents about 20% CO_2 dissolved as $CO_{2,aq}$, 50% dissolved as $HCO_{3,aq}^-$, and 30% precipitated as calcite. The extent of sequestration as HCO_3^- at equilibrium can be calculated from equilibrium thermodynamics and is roughly equivalent to the amount of Na^+ in the initial sandstone in a soluble mineral (here, oligoclase). Similarly, the extent of trapping in calcite is determined by the amount of Ca^{2+} in the initial oligoclase and smectite. Sensitivity analyses show that the rate of CO_2 sequestration is sensitive to the mineral-water reaction kinetic constants between approximately 10

and 4000 years. The sensitivity of CO_2 sequestration to the rate constants decreases in magnitude respectively from oligoclase to albite to smectite.

1. Introduction

Carbon dioxide storage in deep saline reservoirs is one option for mitigation of CO_2 emissions, which are projected to reach 6300 million metric tons of CO_2 equivalent by 2035 (NETL ATLAS, 2010). Deep saline reservoirs in the U.S.A. have been estimated by the U.S. Regional Carbon Sequestration Partnerships to provide the capacity for roughly 20,000 billion metric tons of CO_2 storage (NETL ATLAS, 2010). This storage volume is roughly two orders of magnitude greater than potential CO_2 storage in depleted oil and gas reservoirs. Thus, deep saline reservoirs are a primary long-term focus for geologic CO_2 storage in the U.S.A. In the near term, geological storage of CO_2 in conjunction with CO_2-enhanced oil recovery is increasingly being recognized as an important commercial option for CO_2 capture, utilization, and storage.

Geological CO_2 storage requires an ability to predict the behavior of the geologic system over both the near- and long-term. Near-term behavior includes changes that occur during injection and in the period post-closure when the storage system may be relatively more dynamic, while long-term behavior includes changes during the stewardship phase that lasts from centuries to millennia. Many aspects of CO_2 behavior during injection can be predicted based on historical experience from oil and gas operations, but many of the longer-term effects may require additional investigation. Furthermore, because storage lifetimes must exceed the duration of present-day field tests of CO_2 storage by orders of magnitude, conceptual and numerical models are needed that represent the important geochemical processes. Specifically, models are needed to understand whether injection will effectively sequester the CO_2 for time periods that are long enough to warrant the economic investment, to meet regulations, and to convince the public that storage reservoirs are safe. The U.S. Department of Energy's National Risk Assessment Partnership (NRAP) is focused on developing an integrated assessment model framework that predicts the behavior of rock-water-CO_2 interactions during CO_2 sequestration (Cugini et al., 2010). The integrated assessment model will be a reduced-order model that is derived from detailed process models for key system dynamics. The first generation NRAP risk models have been written under the assumption that geochemical reactions will proceed to equilibrium; however, incorporation of mineral reaction kinetics may be needed in second-generation models to provide accurate representations of CO_2 behavior.

Geochemical calculations are needed to predict reactions that range from dissolution of CO_2 in brines to precipitation of storage-reservoir minerals. Such calculations rely on thermodynamic and kinetic databases which have uncertainty: for example, one problem has been identified with respect to the thermodynamic properties of Fe^{2+} versus Fe^{3+} (Xu et al., 2005). However, the potential uncertainties in kinetic data are even larger than in the thermodynamic databases: the experimental laboratory versus field rates vary by factors up to 10^5 for earth surface systems (White and Brantley, 2003). One of the goals of this paper is to evaluate which mineral

reaction rates affect the type and extent of CO_2 trapping that will occur, and the timescales of these reactions.

To accomplish the goals, a case study consisting of a baseline reservoir + brine is first defined. Ninety percent of sequestration reservoirs in the U.S.A. are likely to be clastic (Wildgust et al., 2011). The temperature (T), pressure (P), mineralogy, and chemistry of the baseline reservoir were chosen so as to represent a rough average of the characteristics of sandstone-hosted reservoirs currently proposed in the U.S.A. for sequestration. Modeling the reactivity of a clastic reservoir is a particular challenge because of the variety of minerals that can be present.

In a generalized CO_2 storage scenario, a CO_2-enriched fluid is injected into a brine-filled sandstone that is bounded on the top (and bottom) by impermeable shale. In this paper, a one-dimensional problem is explored – a diffusion problem which simulates the alteration of one part of the sandstone layer. This reactive diffusion model approximates some of the processes that occur after lateral flow of injected CO_2 has slowed. The model simulation does not include advection in order to focus on the reaction kinetics part of the problem without incorporation of the heterogeneities and complexities that are important in advective transport. The reactive diffusion model allows identification of the rates and extents of water-rock reactions driven by emplacement of CO_2 using rate constants from the published literature. The focus on the reactive diffusion problem and sensitivity tests allowed identification of the minerals which react slow enough to impact the geochemical evolution of storage. The baseline reservoir is proposed here to facilitate future cross-comparisons with other geochemical models.

2. Background

2.1. CO_2 sequestration

Carbon dioxide trapping processes are often divided into four classes (Benson and Cole, 2008; Doughty, 2010). First, CO_2 is stored by *structural trapping* if the CO_2 is largely present as a continuous supercritical phase within a pocket of porous rock that is sealed by a low permeability cap rock. The second process is *capillary* or *residual trapping;* in this case, CO_2 fills discontinuous clusters of water-wet pores and is immobilized. Such residual trapping can fill 15 – 25 % of pore space with supercritical (SC) CO_2 (Benson and Cook, 2005; Doughty, 2010). Third, *solubility trapping* refers to the dissolution of CO_2 in the aqueous solution as species such as $CO_{2,aq}$, $HCO_3^-{}_{,aq}$, or $CO_3^{2-}{}_{,aq}$. Here, $CO_{2,aq}$ stands for the sum of all electrically neutral aqueous forms of dissolved CO_2 including $H_2CO_{3,aq}$. Finally, *mineral trapping* occurs when aqueous CO_2 species precipitate to form carbonate minerals such as calcite, ankerite or dawsonite.

Importantly, these different classes of trapping occur over different timescales. After injection, CO_2 can be structurally trapped almost immediately (within a few years). Residual trapping continues for decades after injection due to two-phase flow driven by buoyancy of the CO_2 (Benson and Cook, 2005; Doughty, 2010). Under favorable structural conditions, residual trapping can immobilize 59 % of the injected CO_2 after only 25 years (i.e., 25 a) (Doughty, 2010). The kinetics of SC CO_2 dissolution into the brine with formation of $CO_{2,aq}$ is also relatively fast: at 25 °C and 30 MPa the rate of dissolution of CO_2 liquid droplets into ocean water equals $6.3\ 10^{-3}$

mol m^{-2} s^{-1} (Shindo et al., 1995). Given this rate, this process will become transport limited. In contrast, the conversion of $CO_{2,aq}$ into $HCO_3^-{}_{,aq}$ is slower because it depends upon the rate of cation (Na^+, Ca^{++}, K^+) release due to mineral dissolution, which neutralizes the H_2CO_3, allowing the dissociation reaction to proceed further. The minerals dissolve and precipitate over timescales of days to tens of thousands of years. Given that the extent of reaction is very much affected by the flow rate of the fluid through the reservoir, the effect of porosity, permeability, and effective diffusion coefficients of reacting species are all important (Balashov, 1995; Oelkers, 1996; Steefel, 2008).

2.2. Saline reservoirs

Currently, there are a number of projects around the world that are in the planning stages for, or have begun injection of, CO_2-laden fluids into deep saline aquifers to test sequestration (Michael et al., 2010; NETL ATLAS, 2010). Deep saline reservoirs considered for sequestration are typically sandstones consisting primarily of quartz, feldspar, carbonate and clay minerals (often pore-filling). The variable mineralogy of these reservoirs is illustrated in Table 1, which summarizes parameters and findings from ten previously published reactive transport modeling studies that have simulated sequestration. Researchers have utilized reactive transport models that include only the important mineral-water-gas reactions.

Within this compilation of reservoirs, the mineralogy and reservoir conditions vary greatly (Table 1). For example, the Mt. Simon sandstone (a unit with projected storage potential of ~150 billion metric tons CO_2; NETL ATLAS, 2010) is generally considered to be a relatively pure quartz arenite. However, within the Illinois basin, that sandstone contains zones of abundant feldspars, clays and carbonate minerals that affect porosity locally (Bowen et al., 2011).

2.3. Previous reactive transport models of sequestration

Although model predictions vary due to differences in inputs (e.g., temperatures ranging from 37 to 75^{o}C) and approaches, some general trends are observed from the models in Table 1. The low pH caused by CO_2 dissolution and hydrolysis cause relatively rapid and early carbonate mineral dissolution. This stage is followed by a period when various silicate minerals dissolve. For example, because of the small grain size and high specific surface area, clay mineral dissolution tends to occur early. Feldspar dissolution occurs throughout these early stages but because feldspars tend to have lower surface area and larger grain size, feldspars persist for much longer.

In the models, dissolution of silicate minerals releases silica to solution which eventually precipitates as Si-containing minerals that can include quartz or opal-A (Xu et al., 2007a). In the final stages, consumption of H^+ by the dissolution reactions raises the pH and CO_2 is converted to $HCO_3^-{}_{(aq)}$. This leads to precipitation of carbonates and clay minerals such as kaolinite, smectite, illite and chlorite. Given the differences in starting mineralogies, brine compositions, model parameters and modeling approaches, it is impossible to ascertain what controls the different clay mineral assemblages predicted by the various models.

Eight out of the nine models predicted the formation of dawsonite ($NaAlCO_3(OH)_2$). In addition, six of the nine models predicted the formation of either

siderite ($FeCO_3$) or ankerite ($(Ca,Mg,Fe)CO_3$) or both. Magnesite, calcite and dolomite were also reported to form in several models, although they were less important for trapping CO_2. Although carbonate precipitation was often predicted, the amount of mineral trapping of CO_2 in each model is difficult to compare from one study to the other because of different choices of units. Based on inspection of the studies, the most practical expression of mineral trapping is summarized in mass CO_2 trapped per m^3 of rock, m_{CO2}. These values ranged from ~17 kg/m^3 to ~90kg/m^3.

3. The baseline case

Only broad generalizations can be made based on Table 1. For example, most of the important mineral transformations barely commence within the first 100 a but are nearly complete within 20 ka. Furthermore, the most important parameters or inputs that affect CO_2 sequestration rates appear to be initial mineralogy, mineral surface area, and the choice of rate constants.

Comparison among models is difficult because of different choices of reservoir characteristics, model approaches, and thermodynamic and kinetic databases. To eliminate one of these types of discrepancy, a baseline case for future simulations is proposed here. It is argued that a key confidence-building step for the use of models of sequestration is to show that multiple models yield consistent predictions. For example, PHREEQC models with different thermodynamic data bases result in variations of a factor of six in the amounts of stored CO_2 (Dethlefsen et al., 2011). They concluded that this discrepancy is due to differences in the tabulated thermodynamic properties of K-feldspar. Here, information is combined from site-specific models with information about the mineralogy, brine chemistry, and physical conditions in deep saline reservoirs from other literature sources to establish a baseline case.

3.1. Geophysical conditions

Mineral reactivity is strongly influenced by temperature and, to a lesser extent, pressure. While temperature affects solubility and reaction kinetics, the confining pressure for a storage reservoir determines the maximum CO_2 pressure attainable. This CO_2 pressure in turn determines the solution pH, which strongly influences reaction rate. Constraints on these parameters are described below.

If storage is targeted for depths below ~0.8 km, CO_2 will exist as a supercritical fluid and will, therefore, require less storage volume. Furthermore, as noted by Stauffer et al. (2009), changes in depth-related properties such as viscosity ratio, density and injection pressures may favor deeper wells both economically and with respect to risk. However, depth must also be considered in terms of drilling costs (Stauffer et al., 2009). Recognizing such trade-offs, it is assumed that reservoir storage depth will most likely be between 1 and 3 km. Given that the average continental geothermal gradient is ~25°C/km (Fig. 1), temperatures will likely range between ~50 and 100°C. It might be reasonable to extend this temperature range up to 125°C because sediments are good insulators and the geothermal gradient in some sedimentary basins might be as high as 35°C/km. Thus, at 3 km depth, T = 130°C. Here, 2 km is chosen as a prototypical depth for the storage reservoir and a temperature of 75°C.

Solutions with a density near 1g /cm^3 are consistent with a hydrostatic pressure gradient of 10 MPa/km (100 bar/km). Likewise, sedimentary rocks with a density of ~2.3 g/cm^3 are consistent with a lithostatic pressure gradient of ~23 MPa/km. However, it is unlikely that storage reservoir pressures will exceed about 65% of lithostatic pressure because rock units tend to hydrofracture if pressurized above this value (Dickinson and Suczek, 1979). This bounds the envelope of CO_2 pressure that could be present in a storage reservoir by an upper limit of 14.5 MPa/km. The upper limit of P_{CO2} in a storage reservoir at a depth of 2 km, 30 MPa (Fig. 1), is, therefore, chosen for the baseline model.

Rock porosity and permeability are the two key physical factors in determining capacity for CO_2 disposal. These parameters are reservoir-specific and can vary significantly within a reservoir. In the context of the diffusion-driven processes considered in this study, permeability is irrelevant; instead tortuosity is the primary factor, for which an idealized value discussed below was used. For porosity, ϕ, a value of 0.25 was chosen as a moderate value for the baseline case.

3.2. Geochemical conditions

For any geochemical simulation, the number of phases and components must be limited. In the present treatment, the chemistry and mineralogy was, therefore, restricted to the eight-component system, SiO_2-Al_2O_3-CaO-Na_2O-K_2O-HCl-CO_2-H_2O and a relatively simple baseline mineralogy (Table 2). To choose the mineralogy, sandstones derived from continental block lithologies were emphasized to avoid complications associated with lithic fragments (Dickinson and Suczek, 1979). The feldspar content of such sandstones has been observed to range up to 50% (Dickinson and Suczek, 1979). The baseline sandstone was, therefore, assumed to contain a total feldspar content of 26% (18% K-feldspar, 8% plagioclase). These values are higher than the previously reported average value of 15% for sandstones (Pettijohn et al., 1987). However, the higher feldspar value is not dissimilar from many observed values. Although plagioclase compositions vary up to An_{70} (Trevena and Nash, 1979), an average value of An_{20} (oligoclase) was chosen because oligoclase is the most common feldspar mineral in surface systems. The average feldspar grain diameter was set to 0.125 mm based on published results (see for example Figure 3 in Odom, 1976). Geometric specific surface areas were assumed for all minerals. Based upon these considerations, the baseline sandstone was set to the mineralogy summarized in Table 2.

The pore fluids in sandstone saline reservoirs are typically dominated by NaCl with significant $CaCl_2$. Values from the most comprehensive compilation of North American oil-field brine compositions were averaged to obtain the modeled concentrations in Table 3 (Collins, 1975). In order to adapt the Collins data to the eight-component system, the Mg concentration for each brine was added to the Ca concentration on a molal basis. Likewise, twice the SO_4^{2-} concentration was added to the Cl^- concentration to yield the values listed in Table 3. The ionic strength of this calculated solution is 2.41 (~14 mass % NaCl equivalent).

4. Reactive transport modeling

The use of a numerical reactive-transport code that incorporated reaction kinetics was explored to investigate the effect of diffusive-reactive partitioning of CO_2 across the interface within the baseline sandstone between supercritical CO_2 and the brine. With this model, sensitivity tests were run to determine which mineral kinetics are important.

4.1. Setup of the reactive diffusion problem

The reactive diffusion process was investigated because it is the slowest of all transport processes. Thus if the kinetics of mineral reactions are important during reactive diffusion, kinetics will also be important for a system with advective transport (for example, convection due to variable brine density). The general setup of the reactive diffusion model is represented in Figure 2. The content of water in the supercritical CO_2 (SC CO_2) phase was assumed to be negligible. Specifically, at 75 °C and 30 MPa, the CO_2 fluid is calculated to contain ~0.6 mass % H_2O at equilibrium with the brine (Duan and Sun, 2003). The solubilities of minerals in this SC CO_2 phase are extremely low. Therefore, the transfer of H_2O, rock, and salt components through interface (A) was disregarded and only diffusion of CO_2 was allowed.

Although the buoyancy of SC CO_2 and its small viscosity will generate a highly dynamic response that includes convection, these are not included in the model. The focus instead is on simulating reactive diffusion which must occur in every situation at certain boundaries as shown in Figure 3. The model, therefore, simulates an element common to all CO_2-injected systems and allows focus on the importance of the kinetics of fluid-rock interactions.

In general it is assumed that CO_2 will be injected into a horizontal layer of sandstone sandwiched between two layers of low-permeability shale (Benson and Cook, 2005). After injection, the supercritical CO_2 plume will be stabilized physically, forming a plume entirely within the sandstone. Computations show that under favorable conditions, such immobilization of SC CO_2 can occur within 25 a of CO_2 injection (Doughty, 2010). The immobilized SC CO_2 is mostly residually trapped, filling relatively disconnected clusters of pores. In principle, under these conditions the plume consists of a heterogeneous region comprised of pores containing the two immiscible phases, SC CO_2 and CO_2–saturated brine. The filling of the pores might have a complex geometry. For example, aqueous and CO_2 fluids will coexist within neighboring pores or even within the same pores in a homogeneous porous medium (Lu et al., 2009; Liu et al., 2010). The details and special features of this heterogeneous region with complex geometry were neglected in the model.

The plume is likely to be shaped somewhat like a funnel with its stem at the injection well within the sandstone reservoir (Benson and Cook, 2005; Dentz and Tartakovsky, 2009; Lu et al., 2009). The plume widens upward to its truncation at the upper caprock. Within the upper part of the plume, the CO_2 diffuses into the shale caprock (Gaus et al., 2005), but this process is not modeled here. At the bottom of the plume, CO_2 diffuses into the brine-saturated sandstone as represented in Figure 3, a schematic which was redrawn after Figure 5.7 in Benson and Cook (2005). Interface (*A*) in Figure 2 defines the sub-horizontal interface of the plume at time 0 between the supercritical CO_2 fluid and the aqueous brine in the sandstone. Interface *A* is

positioned at some distance L_{AB} from the impermeable shale, located at subhorizontal interface *B* (Fig. 2).

The reactive diffusion of CO_2 down into the brine will change brine density and promote convection (Ennis-King and Paterson, 2007). The onset of convection is defined by the Peclet number which describes the balance between diffusion and convection,

$$Pe = \frac{v_c^D L_{AB}}{D} \quad (1)$$

where v_c^D is Darcy velocity for convection, D is the effective diffusion coefficient through porous sandstone, $D = 6\ 10^{-10}$ m^2 s^{-1} (see Supplementary Material), and L_{AB} is the vertical distance from the plume bottom to the lower shale layer (Fig. 3). v_c^D is determined by

$$v_c^D = \frac{k_{sand} \Delta\rho g}{\eta_{brine}} \quad (2)$$

where k_{sand} is sandstone permeability (10^{-15} – 10^{-13} m^2), estimated as 10^{-14} m^2; $\Delta\rho$ (kg m^{-3}) is the brine density increment, $\Delta\rho \propto 0.1$ kg m^{-3}, g is acceleration due to gravity, g =9.8 m s^{-2}, and, the brine viscosity, η_{brine} = 5.2 10^{-4} Pa s (see Supplementary Material).

Using these data and L_{AB}= 30 m, from Equation (1) it is calculated that Pe = 0.93 ≈ 1; and at L_{AB}= 10 m, Pe = 0.31 < 1. On the basis of this estimation, the lower part of the sandstone which is saturated by brine (see Fig. 3) can be thought of as divided into three regions controlled by different transport mechanisms: diffusion, diffusion + convection (labeled in Fig. 3 as the transition zone), and convection. In this paper the zone dominated by diffusion is modeled. Again, the rationale for the focus on diffusion is to be able to determine the importance of the kinetics of fluid-rock interactions. It is likely that reactions that are kinetically limited in the simulation are also kinetically limited in systems that have advective as well as diffusive transport.

4.2. Reactive transport computation

To solve the full reaction – diffusion problem, the program, MK76, was utilized for a heterogeneous system of one aqueous and N_m mineral phases. This program is based on the numerical code that was used previously to solve a transient problem describing reactive diffusion in a weathering system (Lebedeva et al., 2007). MK76 forms and solves the system of differential equations in partial derivatives for reactive diffusion mass transfer (see Supplementary Material).

The aqueous phase is water that contains N_{aq} aqueous solutes. The master variables of the problem are N_p molalities of the primary (independent) aqueous species, plus N_m mineral volume fractions and porosity. Thus there are $N_p + N_m + 1$ variables. The independent chemical components of the system are identical to the primary species. It is assumed that homogeneous aqueous reactions are fast and chemical equilibrium is, therefore, maintained in solution. The secondary species (SC_i) are generated from primary species (PR_k) from mass balance and mass action equations (see Supplementary Material).

The effective diffusion coefficient, *D*, describes diffusion through the porous rock medium, i.e., $D = F_{inv} D^{aq}$, where D^{aq} is the diffusion coefficient in the aqueous pore fluid for all species, and F_{inv} is the inverse of the Archie formation factor for the porous medium ((Balashov, 1995); also see Supplementary Material). Here this factor is approximated by $F_{inv} = \frac{\phi}{\theta_\tau}$, with tortuosity coefficient $\theta_\tau = \pi / 2$ for packed spheres.

I_m is the reaction rate of mineral MNL_m (positive for mineral dissolution),

$$MNL_m \rightleftarrows \sum_{k=1}^{k=N_p} \nu_{mk}^{m} PR_k \qquad m = 1, 2, ..., N_m \tag{3}$$

The rate I_m of a heterogeneous reaction is written following transition state theory according to the following equation which has been reviewed many times in the literature (e.g., Brantley, 2008):

$$I_m = s_m k_m (a_{aq}; \exp(-E_{A,m}/RT))(1 - \exp(-A_m / RT)) \tag{4}$$

In this equation s_m is the specific surface area of mineral *m* ($m^2\ m^{-3}$). It is calculated as the geometric surface area

$$s_m = 6(n_m^g)^{1/3}(\phi_m)^{2/3} \tag{5}$$

where n_m^g (m^{-3}) is the number of mineral grains per unit volume of a porous medium (Table 2) and ϕ_m is the mineral volume fraction. A_m in equation (4) is the chemical affinity of reaction (3) which is included so that rate law (4) describes mineral dissolution if $A_m > 0$ and mineral precipitation if $A_m < 0$. The reaction rate constant k_m is written as $k_m(a_{aq}; \exp(-E_{A,m}/RT))$ because it is a function of a_{aq}, the activity of any species influencing the rate, and $E_{A,m}$, the activation energy of the reaction.

4.3. Kinetic data

The rate laws describing mineral dissolution, Equation (4), were formulated following a published approach (Marini, 2007; Palandri and Kharaka, 2004). The kinetic function for mineral *m* is expressed as the sum of three contributions

$$k_m = k_{H,m} + k_{W,m} + k_{OH,m} \tag{6}$$

where

$$k_{H,m} = a_{H^+}^{n_{H,m}} A_{H,m} \exp\left(-\frac{E_{H,m}}{RT}\right) \tag{7}$$

$$k_{W,m} = A_{W,m} \exp\left(-\frac{E_{W,m}}{RT}\right) \tag{8}$$

$$k_{OH,m} = (b_{H,m} a_{H^+}^{n_{OH,m}} + b_{OH,m} a_{OH^-}^{n_{OH,m}}) A_{OH,m} \exp\left(-\frac{E_{OH,m}}{RT}\right) \tag{9}$$

This approach relies on the use of three activation energies $E_{H,m}$, $E_{W,m}$, and $E_{OH,m}$ for dissolution by the acidic, neutral and basic mechanisms, respectively. In some cases (Palandri and Kharaka, 2004), the basic mechanism is expressed using the term $a_{H^+}^{n_{OH}}$, while in other cases (Brantley, 2008; Köhler et al., 2003) by the term $a_{OH^-}^{n_{OH}}$. For this

reason, in Equation (9) the coefficients b_H and b_{OH} (which equal 0 or 1) have been introduced, in other words, either term can be used (but not both) depending upon how the original authors parameterized their model. The parameters used in Equations (7) - (9) for the model are represented in Table 5. As described later in the text, these kinetic constants were varied over suitable ranges in sensitivity tests to assess how knowledge of the rate constants affected the conclusions. Alternately, because these rate constants are always multiplied by the mineral surface area in the model equations, the sensitivity tests can be thought of as tests of variations in total surface area of the reacting phase.

Note that albite and kaolinite are not present in the initial mineral assemblage although they are allowed to precipitate with no kinetic barriers to nucleation . Furthermore, dawsonite was not allowed to precipitate in this model. Many studies in the past (Table 1) have predicted the formation of dawsonite at CO_2 sequestration conditions; however, as discussed in more detail previously (Kaszuba et al., 2011), dawsonite has rarely been found as a precipitate in natural analog sites or in laboratory studies. In addition, researchers have noted that the largely undetermined growth and nucleation parameters for dawsonite (Pham et al., 2011) result in much of the uncertainty in model simulations related to dawsonite. Given the on-going debate as to whether or not to include dawsonite in modeling of CO_2 storage systems, it was decided to not include it in the secondary mineral assemblage.

5. Modeling Results

5.1. Reaction diffusion models

In discussing the results of the diffusion-reaction calculation, the solution for the problem in Figure 2 with L_{AB} = 3 m is first discussed. Interface A (Fig. 2) was closed for all components except CO_2. The concentration of CO_2 at the boundary was maintained at a constant dissolved $CO_{2,aq}$ value set close to the equilibrium value determined for the supercritical CO_2 phase at 75 °C and 30 MPa ($m^A_{CO2,aq}$= 0.65 mole kg^{-1}). The lower sandstone – shale interface at B was modeled as a no-flow boundary for all species. The diffusion problem was solved for 348.15 K and 30 MPa. The transient solutions were calculated over the interval from 0 to 25 ka at which time the system reached equilibrium.

Initially the pore fluid was assumed to be in chemical equilibrium with the sandstone mineral assemblage and was calculated to have the composition summarized in Table 3. For the 8-component system at the given P-T conditions, the baseline sandstone assemblage of 7 phases (six minerals + one brine), is thermodynamically invariant according to the Gibbs phase rule. Namely, there are 7 phases and 7 mineral components plus one additional component (Cl^-) that does not enter any mineral phase. Its concentration was assumed to be externally determined: Cl^- concentration was set to 2.146 mole kg^{-1} (Table 3). The invariance of this sandstone assemblage means that the initial concentration of dissolved CO_2 is buffered at a small concentration, ~10^{-4} mole kg^{-1}, as summarized in Table 3.

At time zero, the supercritical CO_2 phase was emplaced at boundary A. The profiles of propagation of reacting $CO_{2,aq}$ into the brine in the sandstone and the resultant pH values are shown in Figure 4 where depth down into the sandstone appears as horizontal distance. In the model with L_{AB} = 3 m, ~ 100 a are required for

$CO_{2,aq}$ to reach the underlying shale. In other words, 100 a is the time needed to attain 2/3 of the $CO_{2,aq}$ value maintained constant at boundary A. (Note that 2/3 was chosen as an arbitrary value because any value could have been chosen such as 95%, 99%, etc.)

So far, the choice of the length of sandstone simulated, L_{AB} (see Fig. 2), has not been discussed. By analogy with metamorphic systems (Balashov and Lebedeva, 1989), it is clear that a critical length, L^*_{AB}, exists such that for values $L_{AB} > L^*_{AB}$ (Fig. 2), redistribution of CO_2 from the supercritical phase into the brine and mineral phases will proceed by formation of distinct mineral reaction fronts that approach the limit of local chemical equilibrium, LCE, for reactive diffusion. Here, LCE is the hypothetical case such that the reaction kinetics are fast and chemical equilibrium is everywhere achieved. Theoretically, if $L_{AB} >> L^*_{AB}$, LCE will be attained if diffusion is allowed to proceed for a long-enough period of time. The characteristic time needed to attain the maximum extent of CO_2 sequestration at equilibrium, τ, is a function of L_{AB} and D. It can be shown that $\tau \propto L^2_{AB}/D$ (Balashov and Lebedeva, 1989). For time $> \tau$, the amount of CO_2 stored will not vary with the rate constants of mineral reactions. In contrast, for time $< \tau$, the total amount of CO_2 stored will vary with the rate constants for mineral reactions.

For example, the computations represented in Figure 5 show that for $L_{AB} \leq 3$ m, diffusion-driven redistribution of CO_2 from the plume into the sandstone + brine is controlled by the kinetics of mineral/fluid reactions (i.e., local equilibrium is not attained). Using the results of these computations in combination with data on kinetics and diffusion and the LCE solution for reactive diffusion, it has been shown in the Supplementary Material that $L^*_{AB} \approx 20$ m. Above this critical length, the redistribution (sequestration) of CO_2 into the sandstone will be slowed due to slow rates of diffusion. In contrast, the distribution of phases for all values of $L_{AB} \leq 20$ m are identical (Fig. 5).

A pH gradient forms inside the sandstone only during the first years. This pH gradient is eliminated as the cations -- K^+, Ca^{++}, and especially Na^+ -- are released due to feldspar dissolution and the brine is charge-balanced by formation of HCO_3^-. After 50 a, the pH of the brine is buffered primarily by H_2CO_3 + $NaHCO_3$ (Fig. 4 bottom). The average mineral volume fractions for the 3-m layer are shown as a function of time in Figure 5a. On the left side of the figure the mineral assemblage, Mc + Olg + Cc + Smct + Ill + Qz, is not yet equilibrated with brine + CO_2 and on the right side the assemblage, Mc + Ill + Qtz + Cc is entirely equilibrated with CO_2 + brine.

From a theoretical point of view, reactive diffusion into the sandstone is identical to a classic metamorphic system that is closed with respect to all components except CO_2 which diffuses in through boundary A (Fig. 2). Using published terminology (Korzhinskii, 1936, 1970; Thompson, 1970), CO_2 can be considered a *perfect mobile component*. Given sufficient time, this system reaches a new equilibrium state where the chemical potential of CO_2 (μ^s_{CO2}) in the sandstone equals the chemical potential of CO_2 in the supercritical phase (μ^v_{CO2}) maintained at the interface A.

As shown later (Fig. 8), CO_2 sequestration occurs throughout the reacting system as long as μ^s_{CO2} is changing (see Fig.4). Nonetheless, the sequestration (redistribution)

of CO_2 at ~ 4 ka is very close to its maximum value. At this time, at a position 3 m from the plume, the CO_2 chemical potential in the sandstone is approximately equal to the value externally applied at interface A, μ^{v}_{CO2}. After 4 ka, the sluggish reactive process continues in the sandstone under SC CO_2 buffered conditions until complete equilibrium is attained at ~25 ka. The duration of time from 4 to 25 ka is necessary for illite to completely replace kaolinite (Chermak and Rimstidt, 1990).

After a short induction time (<50 a), concentration of $CO_{2,aq}$ is significant across the entire simulation volume (Fig. 4). After 1000 a, very little change in this concentration is observed; however, as shown in Figure 6, the concentration of HCO_3^- increases significantly as albite dissolves to increase dissolved Na^+. However, the pH does not change significantly during this latter alteration process because the system is strongly buffered: from the initial value ≈ 7.2, pH decreases to 5 after 200 a, but increases again to 6 after that (Fig. 6). The saturation indices, log (Q/K_{eq}), for minerals also vary significantly over time (Fig. 6, bottom). Here Q and K_{eq} are the ion activity product and equilibrium constant for each mineral dissolution reaction. Figure 6 (bottom panel) shows that calcite and microcline are always at or near chemical equilibrium because of the fast kinetics of calcite (Fig. 7) and the relatively low microcline solubility in comparison with Na feldspars. For the simulations, quartz is in equilibrium with the initial brine and with the final brine + CO_2 fluid. However, between 50 and 5000 a, the pore fluid is supersaturated with respect to quartz as shown in Figure 6.

The remarkable feature of Figure 6 (bottom) (in conjunction with Fig. 5) is that three minerals (smectite, albite and kaolinite) are dissolved close to LCE within the time spans 60 – 800, 200 – 3,500, and 3,000 – 20,000 a, respectively. Immediately after complete dissolution, the saturation indices of these minerals decrease precipitously. This feature means that the reactive system evolves through a series of steps, termed kinetic stationary states.

Observations from Figures 5 and 6 are summarized in Table 5. Reactive diffusion of $CO_{2,aq}$ dissolves oligoclase until dissolution is complete by ~ 100 a. As Ca is released from oligoclase, two other Ca-containing minerals - calcite and, especially, smectite, precipitate. The smectite precipitation is promoted by supersaturation due to silica release during oligoclase dissolution. After ~50 a, the precipitation of albite and kaolinite become significant; at that point, smectite begins to dissolve close to LCE. Smectite disappears by 800 a. After 4000 a, illite begins to grow at the expense of kaolinite and microcline.

With respect to mineral or solubility trapping of CO_2, the system is controlled most directly by the reactions of oligoclase, smectite and albite. Specifically, trapping of CO_2 is determined by dissolution of oligoclase, by the replacement of smectite by calcite, and by the transformation of albite to kaolinite. The first two reactions control concentrations of Ca in solution (which controls mineral trapping) and the latter reaction controls the conversion of $CO_{2,aq}$ into $HCO_3^-{}_{,aq}$ (solubility trapping). By ~ 3500 a, the albite disappears and CO_2 mineral trapping reaches its maximum. Although mineral trapping of CO_2 stops by 1000 a and $HCO_3^-{}_{,aq}$ trapping essentially stops by 3500 a, the very slow kinetics of kaolinite + microcline replacement by illite determines the rate of final equilibration to Mc+Ill+Cc+Qtz, which is achieved only

by 25,000 a. During this process there is additional small HCO_3^- trapping because of the growth in aqueous $KHCO_3$ concentration (Fig. 8).

6. Discussion of Model Results

6.1. Rationale for mineral choices in the baseline model

The baseline model presented in this paper was designed to simulate the most important geochemical reactions that will occur in a deep saline CO_2 reservoir. However, the simplicity and power of the model comes at the cost of ignoring less abundant minerals. The rationale for incorporating minerals in the model is highlighted in Figure 7 which compares the reactivity at 75°C of minerals commonly found in clastic sediments. Minerals have been divided into broad classes in the four diagrams. The approximate effects of temperature on the dissolution rates are shown by the nomogram on the feldspar figure. That nomogram is based on an approximation that the activation energy for all the dissolution reactions is 65 kJ/mol. It shows that reducing the temperature to 50°C will lower the reaction rates by about 0.75 log units. Raising the temperature to 100°C will increase the reaction rates by about 0.65 log units and raising the temperature to 125°C will increase the reaction rates by about 1.22 log units over the 75°C rates.

Figure 7 shows that using the dissolution rate for oligoclase to approximate the behavior of the Na-rich plagioclase feldspars, as we has been done here, is reasonable because the rates of dissolution of the plagioclase compositions from albite to andesine lie reasonably close to oligoclase. Furthermore, because the more Ca-rich plagioclase feldspars are likely to be destroyed by chemical weathering, their abundance is low in most clastic sediments. In contrast, the dissolution rate of K-feldspar (e.g., microcline) is significantly slower than the dissolution rate of oligoclase and so it is necessary to incorporate it explicitly as a phase. The intrinsic dissolution rate of the feldspar minerals ranges between $10^{-9.5}$ to $10^{-11.5}$ mol/m^{2}sec over the pH range of 3 to 8. Although this rate is fairly low, the relatively high abundance of feldspars in sandstones make them potentially important reactants in CO_2-charged waters. Indeed, as discussed previously and below, CO_2 dissolution trapping is largely dictated by the feldspar reactions in clastic systems.

Kaolinite, smectite, and illite are also reasonably abundant in clastic rocks because they are weathering products of the feldspars – hence they were incorporated here. These clays can be present in minor to moderate abundance in sandstones; however, their small grain size and high specific surface area offsets their low intrinsic reactivity, allowing them to play an important role in storage-reservoir chemistry. In fact, it is the clay reactions that take the longest time to equilibrate in the reservoir (Figs 5, 6, Table 5). These clay minerals each display distinct dissolution behaviors as a function of pH and thus must be incorporated explicitly in a reservoir model. By comparison, chlorite and glauconite are very reactive and are usually rapidly destroyed by chemical weathering and not commonly found in sandstones; therefore, those minerals were not incorporated into the baseline sandstone.

Calcite is the most abundant carbonate mineral found in clastic rocks but dolomite, siderite and ankerite can be locally abundant. Even when considerably less abundant than silicate minerals, carbonates are so reactive that they play an important role in sequestering CO_2. Note that the dissolution rates of dolomite and calcite are

relatively similar, so lumping dolomite and calcite together in a model is a reasonable approximation. Likewise, the expected siderite and ankerite dissolution rates are similar to those of calcite and dolomite. Furthermore, the dissolution rates of all those minerals are fast enough that they may become transport-limited. Although present as minor constituents of clastic rocks, carbonates have high intrinsic reactivity and are very important players in the early stages of CO_2 injection.

Quartz, a mineral which is ubiquitous and highly resistant to chemical weathering, is by far the most abundant oxide/hydroxide mineral in clastic rocks. Even though quartz dissolution rates are very slow (Fig. 7), quartz is the most important long-term buffer for dissolved silica concentrations in pore waters because it is so abundant. This buffer controls the solubility of the other silica-bearing phases so it will affect the long-term evolution of all CO_2 injection sites. Quartz is also important in that it provides a framework that holds open porosity while other minerals dissolve or precipitate. Iron and Al oxyhydroxide phases, not incorporated into the baseline sandstone, are always less abundant than quartz and are expected to play a rather minor role in most storage-reservoir processes.

6.2. Evolution of CO_2 sequestration

Carbon dioxide diffusion into the brine-saturated sandstone is essentially an acid-base titration: the acid is the H_2CO_3 formed as CO_2 gas dissolves in the aqueous fluid and the base is the rock itself. Therefore, during the reactive diffusion, CO_2 is stored by three mechanisms: 1) dissolution of CO_2 into aqueous brine ($CO_{2,aq}$); 2) hydration and deprotonation of CO_2 to form HCO_3^- (+ minor CO_3^{2-}); 3) precipitation of calcite. Mechanisms (1) and (2) comprise solubility trapping while mechanism (3) comprises mineral trapping. Furthermore, mechanism (1) is simply dissolution of the CO_2. In contrast, mechanism (2) is the acid-base titration of Na,Ca,K-silicates dissolving into water-CO_2 to form HCO_3^- + CO_3^{2-} ions that charge-balance the hard cations, Na, Ca, K. This solubility trapping is largely due to dissolution of feldspars - in particular, Na feldspars. Notably, although the details of these processes will depend upon the exact mineralogy of the sandstone reservoir, the overall trends noted here will be true for most systems.

The average concentrations of stored CO_2 in moles per m^3 sandstone by the three different mechanisms were calculated for the model with L_{AB} = 3 m to yield what are called here the *standard curves* shown in Figure 8. These were computed with the *standard* set of kinetic constants of mineral dissolution/ precipitation (Table 4). Figure 8 shows that CO_2 sequestration was complete to within 97% of the maximum value by 3500 a. After 3500 a, the main mechanism by which HCO_3^- forms, i.e., albite transformation to kaolinite + quartz, ceases:

$$2CO_2 + 3H_2O + 2Ab \rightleftharpoons 2Na^+ + 2HCO_3^- + Kln + 4Qtz \qquad (10)$$

For t > 3500, the main alteration reaction is the replacement of kaolinite by illite to form the equilibrium assemblage Qtz + Cc + Mc + Ill. During that last process, the CO_2 chemical potential inside the sandstone equilibrates to the chemical potential of CO_2 in the gas plume at the interface A. Thus the last 3% of the total CO_2 is stored as HCO_3^- during the last stage of sandstone alteration as microcline dissolves to form aqueous $KHCO_3$. This last stage occurs under conditions of so-called "perfect mobile CO_2 behavior" (Korzhinskii, 1970).

For the baseline sandstone, the maximum amount of stored CO_2, $[CO_2]_{\max}$, equals 784 mole per m^3 of sandstone (Fig. 8), or 34.5 kg CO_2 per sandstone m^3. This quantity defines the absolute capacity of the saline baseline sandstone reservoir for CO_2 sequestration. This maximum is comprised of 21% CO_2 dissolved as $CO_{2,aq}$, 49% dissolved as HCO_3^-, and 30% precipitated as calcite, i.e., 70% solubility trapping and 30% mineral trapping. The extent of sequestration as HCO_3^- is mainly determined by the amount of Na^+ in the initial sandstone in the soluble Na-containing mineral (here, oligoclase); in contrast, the extent of trapping in calcite is determined by the initial content of soluble Ca-silicates (here, oligoclase and smectite). These final solubility:mineral trapping ratios do not depend upon the reactive transport model but rather can be readily calculated from the initial sandstone composition if the initial and final equilibrium states of the thermodynamic system are calculated. The reactive transport model determines the paths of evolution between initial and final states.

The efficiency of CO_2 redistribution from the CO_2 plume into the saline reservoir can be defined as the ratio of $[CO_2]_{\max}$ to the mass of SC CO_2 in reservoir pores at full saturation (= 1) by SC CO_2. Here $[CO_2]_{\max}$ equals 34.5 kg m^{-3}. The density of SC CO_2, ρ_{CO2}^{sc} = 760 kg m^{-3}, at 75 °C and 30 MPa, means that the maximum mass of SC CO_2 per m^3 is $[CO_2]_{tot}^{sc} = \rho_{CO2}^{sc}\phi$ = 190 kg m^{-3} for the baseline sandstone with porosity ϕ = 0.25. The baseline sandstone efficiency ratio is, therefore, $[CO_2]_{\max} / [CO_2]_{tot}^{sc}$ = 0.18.

6.3. Kinetic sensitivity analysis

The kinetic sensitivity analysis is divided into two parts. In the first part the focus is on the impact of kinetic rate constants on stored CO_2 (in units of moles CO_2/ m^3 of brine-saturated sandstone). The second part concentrates on the time sequence of important controlling minerals, i.e., rates of appearance (albite) and disappearance (oligoclase, smectite, albite). The minerals appear and disappear to define mineral "waves" that either propagate from the plume boundary to the shale boundary or the reverse. To determine the sensitivity of the models to choice of rate constants for smectite, oligoclase and albite, sensitivity tests were run for L_{AB} = 3 m for a sandstone at 75 °C and 30 MPa. As discussed above, reactive-diffusive CO_2 sequestration in this model does not depend on L_{AB} for $L_{AB} < L_{AB}^* \cong 20$ m.

By summing the three curves in Figure 8, the total CO_2 stored in the brine portion of the reservoir is calculated as a function of time (bottom panel in Fig. 8). Different choices of mineral rate constants were explored to determine how they change the total CO_2 stored (Fig. 9). The results are reported by summarizing the *sensitivity factor*, $[CO_2]^{var} / [CO_2]^{std}$, where $[CO_2]^{std}$ is the mass of CO_2 per m^3 of reservoir stored in the standard model (Table 4) and $[CO_2]^{var}$ is the same mass calculated with variations in the rate constants. The variations in kinetic constants sometimes do and sometimes do not change the path; of course, these variations never change the final value (Fig. 9).

For example, for a 10x increase in the smectite rate constant, the total sequestration curve does not change at all (compare the dashed and dotted lines in Fig. 9, bottom). In contrast, a 100x decrease in smectite rate constant (dash/dotted

line) leads to a decrease in the total CO_2 stored over the interval from 10-150 a by a sensitivity factor of 0.85, to an increase in CO_2 stored during 150-1000 a by a sensitivity factor of 1.2, and, finally, to a decrease in sequestration from 1000 – 4000 a by a factor of 0.9. The maximum deviation in stored CO_2 compared to the standard curve equals ~ 80 mole m^{-3} (Figs 8 - 9). Figure 9 also shows that changes in the rate constants for oligoclase and albite affect CO_2 storage more than that of smectite, especially in the interval 10 – 200 a.

The extent of CO_2 stored by the different mechanisms also changes with time when the rate constants for mineral reactions are changed (Figs 10 - 12). A 10x decrease in the oligoclase rate constant increases the $CO_{2,aq}$ stored from 2 – 80 a (Fig. 10). In contrast, a 10x increase in the oligoclase rate constant leads to a decrease in stored $CO_{2,aq}$ in the 20-100 a interval (Fig. 10). If the oligoclase rate constant is 10x faster, more of the CO_2 is precipitated as calcite from 10- 100 a. These individual effects are larger than the summed total effect (Fig. 9) because of compensation effects (Fig. 10).

These observed compensation effects are kinetic in nature and can be explained qualitatively. For example, consider a 10x increase in the oligoclase (Olg) kinetic constant. In the time interval 0 – 10 a, it leads to higher aqueous concentrations of Na^+ and silica due to oligoclase dissolution; the higher $[Na^+]$ leads to an increase of $[HCO_3^-]$, and higher silica promotes more intensive smectite precipitation which decreases calcite precipitation (Fig. 10). Note that here and throughout, [x] refers to concentration of species *x* in solution. In the time interval 10 – 60 a, albite precipitation decreases $[HCO_3^-]$ and aqueous silica, which in turn decreases smectite precipitation. This then in turn promotes an increase in calcite precipitation (Fig. 10).

In contrast to oligoclase, a 10x increase in the albite rate constant decreases the total CO_2 stored from 30 – 110 a (Fig. 9), but the effect is not large. The effects of changes in the albite rate constant on CO_2 storage by the three mechanisms are broken out in Figure 11. Again, these independent effects are bigger than the total summed effect (Fig. 9), because of strong compensation (Fig. 11). For example, in the time interval 20 – 100 a, a 10x decrease in the Ab kinetic constant leads to higher aqueous concentrations of Na^+ and silica; the higher $[Na^+]$ leads to an increase of $[HCO_3^-]$, and higher silica promotes more intensive smectite precipitation which decreases calcite precipitation (Fig. 11).

A decrease in the smectite kinetic constant significantly affects sequestration as HCO_3^- and as calcite (mineral trapping, Fig. 12). However, these individual effects are each larger than the total summed effect (Fig. 9) because of kinetic compensation (Fig. 12). In fact, a slower smectite rate constant shifts the sequestration to calcite precipitation around the 100 a mark, but lowers the amount of calcite precipitated at 1000a.

The sensitivity analysis shows that CO_2 sequestration is sensitive to the mineral rate constants, decreasing in sensitivity in the following order: oligoclase > albite > smectite. Furthermore, the effect of the smectite rate constant is only significant if the rate constant decreases, whereas for the feldspars, either an increase or a decrease impacts the sequestration. In brief, the importance of the rate constant for albite is related to solubility trapping by formation of $HCO_{3,aq}^-$ (i.e., albite dissolution releases aqueous Na) while the importance of the rate constant for smectite is related to

mineral trapping by formation of calcite (i.e. smectite dissolution releases aqueous Ca). The rate constant for oligoclase is important for both solubility and mineral trapping because oligoclase releases both Na and Ca to solution.

6.4. Time sequences of mineral reaction: sensitivity to rate constants

The sensitivity with respect to kinetics can also be explored by looking at mineral concentration profiles (Figs 13 – 14) for different times. At higher values of the smectite kinetic constant and for time < 80 a (Fig. 13), smectite precipitates as an intensive wave that is maximized at x = 0. Precipitation reaches the maximum concentration at ~ 80 a. After 80 a, the smectite wave propagates backward as smectite dissolves. A 100x decrease in the smectite kinetic constant suppresses this effect. In contrast to smectite, the oligoclase profiles (Fig. 13) show only a dissolution wave that propagates in the forward direction.

Smectite precipitation is promoted by the high concentration of dissolved silica that is caused largely by oligoclase dissolution, whereas smectite dissolution is conditioned by the decrease in alumina concentration caused by albite precipitation. A similar coupling with respect to dissolution/precipitation of smectite and feldspars through dissolved silica concentrations was observed in computations of mineral profiles in soils during continental weathering (Goddéris et al., 2010).

The albite profiles plotted in Figure 14 show that the albite precipitation waves propagate backward while the dissolution waves propagate forward. Of course, these directions are actually upward and downward respectively within the context of the actual system (Fig. 2,3). In general the gradient of mineral concentrations reflects the gradient of the chemical potential of CO_2 through the sandstone layer.

6.5. Mineral reaction networks

The reactive interaction among minerals is summarized in Figure 15 and through comparison of Figures 5, S1 – S3 (Supplementary Material). For example, an increase in the oligoclase kinetic constant is coupled positively to smectite and albite: as the reaction rate of oligoclase increases, the maximum concentration of both smectite and albite also increase. (Likewise, a decrease in the oligoclase kinetic constant decreases the maximum concentrations of smectite and albite.)

In contrast, an increase in the albite kinetic constant is coupled negatively to smectite: as the albite rate constant increases, the maximum predicted concentration of smectite decreases. Likewise, a decrease in the albite kinetic constant increases the maximum concentration of smectite. Furthermore, smectite and albite demonstrate the effect of a positive kinetic auto-response; an increase in the value of their kinetic constants leads to an increase in their maximum predicted concentrations (Fig. 15b).

The observed kinetic coupling among minerals is explained by the non-linearity of the kinetic law, i.e., Equation (4). The rate of mineral reaction is proportional to the product of the kinetic constant times the deviation from equilibrium. This deviation from equilibrium is a non-linear function of the dissolved concentrations of mineral components. These concentrations change in the complex reactive system when the kinetic constants are varied. The aqueous concentrations serve to couple responses among the various minerals.

7. Conclusions

To build confidence in the ability to predict the mechanisms and rates of CO_2 sequestration in the subsurface, models of dissolution of CO_2 into aqueous brines and mineral-brine-CO_2 reactions are needed. Running such models requires kinetic and thermodynamic databases as well as data for reservoirs and formation fluids. Many reactive transport models are available and several researchers have modeled individual systems. To understand and evaluate the models, a baseline sandstone reservoir is proposed that can be modeled by any such reactive transport code. If many researchers model CO_2 interactions for this baseline model, this would allow for systematic comparisons between models in order to learn what behaviors are well-predicted or which behaviors are model-dependent. Furthermore, by focusing on reaction + diffusion (without advection), the important effects, if any, of the kinetics of mineral reaction can be isolated.

The baseline sandstone has 8 chemical components and 6 minerals and is filled with a Na-Ca-Cl brine. The reactive diffusion of CO_2 into this brine is modeled until chemical equilibrium is achieved. The reaction transport model shows that for the first ~30 a of the process, CO_2 is mostly trapped in the solution as $CO_{2(aq)}$ with very little mineral trapping. From 200 to 1000 a, replacement of oligoclase by smectite is accompanied by trapping of some CO_2 in calcite. In addition, dissolution of albite over the time scale of thousands of years results in significant solution trapping of CO_2 as HCO_3^-. After about 4000 a, the chemical potential of CO_2 in the brine matches the chemical potential of CO_2 in the supercritical phase and equilibrium with respect to CO_2 is essentially established. However, mineral equilibration is ongoing for 25,000 a, during which time the final mineral assemblage, quartz-illite-calcite-microcline, is reached. This is consistent with the results of White et al. (2005) who report no further change in reservoir mineralogy after 10 ka for a model run at 54°C.

In the model, 97% of the maximum CO_2 sequestration, 34.5 kg CO_2 per m^3 of sandstone, is attained by 4000 a even though the system does not achieve chemical equilibrium until ~25,000 a. The maximum represents about 20% CO_2 dissolved as $CO_{2(aq)}$, 50% dissolved as HCO_3^-, and 30% precipitated as calcite: 70% solubility trapping versus 30% mineral trapping. The extent of sequestration as HCO_3^- at equilibrium can be calculated from equilibrium thermodynamics without reactive transport modeling because it is mainly determined by the amount of Na^+ in the initial sandstone in a soluble mineral (here, oligoclase); in contrast, the extent of trapping into calcite is determined by the initial content of a soluble Ca-containing silicate (here, oligoclase + smectite). This powerful observation may be generally true for most lithologies and should be explored in other simulations for other systems.

The investigation of the effect of changing the reaction rate constants for smectite, oligoclase and albite showed that increasing constants by 10x for smectite and albite has relatively little effect on the reaction transport model (Fig. 9). This is because smectite was already close to local equilibrium in the standard model (Fig. 6, bottom), and increasing the kinetic constant simply moved the mineral closer to local equilibrium with the brine. In contrast, reducing the albite rate constant by 10x affected the timing of mineral appearance as well as the amount of CO_2 stored by mineral or solution trapping from approximately 10-1000 a. In effect, because the

albite reaction operates in the kinetic regime, the evolution of CO_2 trapping is a function of the rate constants.

Geochemical models generally do not contain all the minerals present in a natural system and the current model is no exception. Nonetheless, model simulations are useful. For example, other workers (Xu et al., 2005) have performed sensitivity analyses to explore the effect of changing kinetic constant of dawsonite, a mineral not included in the present simulations. They numerically investigated the sequestration of CO_2 at the sandstone/shale interface. They found that decreases in the dawsonite kinetic reaction constant by two or three orders of magnitude only resulted in relatively small decreases (ca. 10%) in the CO_2 sequestration. The effect of the kinetic constant was damped because precipitation of dawsonite requires reactants whose availability is controlled by the dissolution of aluminosilicate minerals. This last observation is in good correspondence with the present study. Here, the calcite was practically at local equilibrium with the brine and the rate of calcite precipitation, therefore, depended solely on the available reactive sources of Ca^{2+}. In turn, the reactive sources of Ca^{2+} were determined by oligoclase dissolution and smectite precipitation/dissolution. Furthermore, changing the kinetic constants for one or a few minerals changes the reaction pathways leading to the equilibrium condition but does not change the final equilibrium condition, which is controlled by the system composition, temperature, and pressure only.

The sensitivity studies reported here are consistent with the conclusion that variations in reaction rates mostly affect storage-reservoir behavior in the 10-1000 a time frame. Although the modeling did not include advection, these conclusions about the importance of kinetics from $10\text{-}10^4$ a should also be true for systems that include advection + diffusion because kinetic limitation should be even more important in advective systems.

The reactive diffusion modeling revealed that the kinetics of oligoclase, albite, and smectite are all significant for sequestration and thus are phases that should be considered for any second-generation models of CO_2 storage. The modeling furthermore demonstrates that the behavior of all components is interconnected. Therefore, predicting exact timescales for CO_2 trapping will not be possible given the impossibility of fully constraining all heterogeneities and mineral distributions in the subsurface.

Given this impossibility, it is important to understand broad controls on the sequestration. The reaction transport model described in this paper, along with the modeling results from previous studies, show that the most important mineral-brine reactions are those that consume H^+ ions and thus raise the pH: CO_2 storage is essentially an acid (CO_2) – base (rock) titration. For most reservoirs, the important acid-base reactions will generally include dissolution of feldspar. With the rise in pH, more CO_2 can dissolve in the brine as $HCO_{3\,aq}^-$ which results in an increase in solution trapping. In addition, with time the brine will tend to be less aggressive toward the caprock and/or the cement seal, potentially reducing the chance of reservoir leaks.

Current first-generation risk assessment approaches are based on chemical equilibrium and utilize reduced-order models based on detailed process models to capture dynamics of a system. In order to proceed to second generation, non-equilibrium based models, there is a need to understand which mineral reaction

kinetics affect the sequestration especially over 20 – 100 a time-frames. The results point to the importance of feldspar and clay reaction kinetics over the timeframe 10-10,000 a. Future efforts will be focused on specific flow/reaction rate regimes in which kinetics are an important consideration of storage system performance.

Acknowledgements

This technical effort was performed in support of the National Energy Technology Laboratory's ongoing research in Carbon Storage under the RES contract DE_FE0004000. We thank M. Lebedeva for use of the reactive numerical code for MK76 development, and also, C. Anderson for help with figures. We also are thankful to two anonymous reviewers for their useful critical comments and suggestions to improve manuscript.

References

Audigane, P., Gaus, I., Czernichowski-Lauriol, I., Pruess, K. and Xu, T., 2007. Two-dimensional reactive transport modeling of CO_2 injection in a saline aquifer at the Sleipner Site, North Sea. Am. J. Sci. 307, 974-1008.

Balashov, V.N., 1995. Diffusion of electrolytes in hydrothermal systems: Free solution and porous media. In: Shmulovich, K.I., Yardley, B.W.D., Gonchar, G.G. (Eds), Fluids in Crust: Equilibrium and Transport Properties. Chapman & Hall, London, 215 - 251.

Balashov, V.N., Lebedeva, M.I., 1989. On transition to local equilibrium during development of diffusion bimetasomatic zone. Doklady Akad. Nauk SSSR 307, 703-707.

Benson, S., Cook, P., 2005. Chapter 5: Underground geological storage. In: Metz, B. (Ed.), IPCC Special Report on Carbon dioxide Capture and Storage. Cambridge, U.K., 195-276.

Benson, S.M., Cole, D.R., 2008. CO_2 sequestration in deep sedimentary formations. Elements 4, 325-331.

Bowen, B. B., Ochoa, R. I., Wilkens, N. D., Brophy, J. B., Lovell, T. R., Fischietto, N., Medina, C. R., and Rupp, J. A., 2011. Depositional and diagenetic variability within the Cambrian Mount Simon Sandstone: Implications for carbon dioxide sequestration. Environ. Geosci. 18(2), 69-89.

Brantley, S.L., 2008. Kinetics of mineral dissolution. In: Brantley, S.L., Kubicki, J.D., White, A.F. (Eds), Kinetics of Water-Rock Interaction. Springer, 151 - 210.

Chermak, J.A., Rimstidt, J.D., 1990. Hydrothermal transformation rate of kaolinite to muscovite/illite. Geochim. Cosmochim. Acta 54, 2979-2990.

Collins, A.G., 1975. Geohemistry of Oilfield Waters. Elsevier, Amsterdam.

Cugini, A., Guthrie, G., DePaolo, D., Friedmann, J., and Virden, J., 2010. US-DOE's National Risk Assessment Program: Bridging the Gap to Provide the Science Base to Ensure Successful CO_2 Storage. International Conference on Greenhouse Gas Technologies (GHGT), Wednesday, September 22, Session 7C: Risk Assessment

Dentz, M., Tartakovsky, D.M., 2009. Abrupt-Interface Solution for Carbon Dioxide Injection into Porous Media. Transport Porous Media 79, 15 - 27.

Dethlefsen, F., Haase, C., Ebert, M., Dahmke, A., 2011. Effects of the variances of input parameters on water-mineral interactions during CO_2 sequestration modeling. Energy Procedia 4, 3770-3777.

Dickinson, W.R., Suczek, C.A., 1979. Plate tectonics and sandstone compositions. Am. Assoc. Petrol. Geolog. Bull. 63, 2164-2182.

Doughty, C., 2010. Investigation of CO2 Plume Behavior for a Large-Scale Pilot Test of Geologic Carbon Storage in a Saline Formation. Transport Porous Media 82, 49-76.

Duan, Z., Sun, R., 2003. An improved model calculating CO2 solubility in pure water and aqueous NaCl solutions from 273 to 533 K and from 0 to 2000 bar. Chem. Geol. 193, 257-271.

Ennis-King, J., Paterson, L., 2007. Coupling of geochemical reactions and convective mixing in the long-term geological storage of carbon dioxide. Internat. J. Greenhouse Gas Control 1, 86-93.

Gaus, I., Azaroual, M., Czernichowski-Lauriol, I., 2005. Reactive transport modelling of the impact of CO_2 injection on the clayey cap rock at Sleipner (North Sea). Chem. Geol. 217, 319-337.

Goddéris, Y., Williams, J.Z., Schott, J., Pollard, D., Brantley, S.L., 2010. Time evolution of the mineralogical composition of Mississippi Valley loess over the last 10 kyr: Climate and geochemical modeling. Geochim. Cosmochim. Acta 74, 6357 - 6374.

Gunter, W.D., Perkins, E.H., Hutcheon, I., 2000. Aquifer disposal of acid gases: modelling of water-rock reactions for trapping of acid wastes. Appl. Geochem. 15, 1085-1095.

Johnson, J.W., Nitano, J.J., Knauss, K.G., 2004. Reactive transport modeling of CO_2 storage in saline aquifers to elucidate fundamental processes, trapping mechanisms, and sequestration partitioning. In: Baines, S.J., Worden, R.H. (Eds), Geologic Storage of Carbon Dioxide Geol. Soc. London Spec. Pub. 233 , 107-128.

Johnson, J.W., Nitano, J.J., Steefel, C.I., Knauss, K.G., 2001. Reactive transport modeling of geologic CO_2 sequestration in saline aquifers: the influence of intra-aquifer shales and the relative effectiveness of structural, solubility, and mineral trapping during prograde and retrograde sequestration. First Nat. Conf. Carbon Sequestration. National Energy Technology Laboratory. NETL, Washington D.C.

Kaszuba, J.P., Viswanathan, H.S. and Carey, J.W., 2011. Relative stability and significance of dawsonite and aluminum minerals in geologic carbon sequestration. Geophys. Res. Lett. 38, L08404

Knauss, K.G., Johnson, J.W., Steefel, C.I., 2005. Evaluation of the impact of CO_2, co-contaminant gas, aqueous fluid and reservoir rock interactions on the geologic sequestration of CO_2. Chem. Geol. 217, 339 - 350.

Köhler, S.J., Dufaud, F., Oelkers, E.H., 2003. An experimental study of illite dissolution kinetics as a function of pH from 1.4 to 12.4 and temperature from 5 to 50°C. Geochim. Cosmochim. Acta 67, 3583-3594.

Korzhinskii, D.S., 1936. Mobility and inertness of components in metasomatosis. Izv. Acad. Nauk SSSR, Ser. Geol. No.1, 58 - 60.

Korzhinskii, D.S., 1970. Theory of Metasomatic Zoning. Clarendon Press.

Lebedeva, M.I., Fletcher, R.C., Balashov, V.N., Brantley, S.L., 2007. A reactive diffusion model describing transformation of bedrock to saprolite. Chem. Geol. 244, 624-645.

Liu, F., Lu, P., Zhu, C. and Xiao, Y., 2011. Coupled reactive flow and transport modeling of CO_2 sequestration in the Mt. Simon sandstone formation, midwest U.S.A. Internat. J. Greenhouse Gas Control 5, 294-307.

Liu, Y., Wang, L., Yu, B., 2010. Sharp Front Capturing Method for Carbon Dioxide Plume Propagation during Injection into a Deep Confined Aquifer. Energy Fuels 24, 1431 - 1440.

Lu, C., Lee, S.-Y., Han, W.S., McPherson, B.J., Lichtner, P.C., 2009. Comments on "Abrupt-Interface Solution for Carbon dioxide Injection into Porous Media" by M. Dentz and D. Tartakovsky. Transport Porous Media 79, 29 - 37.

Marini, L., 2007. Geological Sequestration of Carbon Dioxide. Developments in Geochemistry 11. Elsevier, Amsterdam.

Michael, K., Golab, A., Shulakova, V., Ennis-King, J., Allinson, G., Sharma, S., and Aiken, T., 2010. Geological storage of CO2 in saline aquifers - A review of the experience from existing storage operations. Internat. J. Greenhouse Gas Control 4, 659-667.

NETL ATLAS, 2010. Carbon Sequestration Atlas of the United States and Canada. National Energy Technology Laboratory, U.S. Department of Energy.

Odom, I.E., 1976. Nature of feldspar-grain size relations in some quartz-rick sandstones. J. Sed. Petrol. 46, 862 - 870.

Oelkers, E.H., 1996. Physical and chemical properties of rocks and fluids for chemical mass transport calculations. In: Lichtner, P. C., Steefel, C. I., Oelkers, E.H., (Eds), Reactive Transport in Porous Media. Reviews in Mineralogy 34, 131 - 191.

Palandri, J.L., Kharaka, Y.K., 2004. A compilation of rate parameters of water-mineral interaction kinetics for application to geochemical modeling. U.S. Geol. Surv. Open File Report 2004-1068.

Pettijohn, F.J., Potter, P. E., Siever, R., 1987. Sand and Sandstone. Springer-Verlag, New York.

Pham, V.T.H., Lu, P., Aagaard, P., Zhu, C., Hellevang, H., 2011. On the potential of CO2–water–rock interactions for CO2 storage using a modified kinetic model. Internat. J. Greenhouse Gas Control 5, 1002 - 1015.

Shindo, Y., Fujioka, Y., Takeuchi, K., Komiyama, H., 1995. Kinetics on the Dissolution of C02 into Water from the Surface of CO2 Hydrate at High Pressure. Internat. J. Chem. Kinetics 27, 569-575.

Stauffer, P.H., Viswanathan, H.S., Pawar, R.J., Guthrie, G.D., 2009. A system model for geologic sequestration of carbon dioxide. Environ. Sci. Technol. 43, 565 - 570.

Steefel, C.I., 2008. Geochemical kinetics and transport. In: Brantley, S.L., Kubicki, J.D., White, A.F. (Eds), Kinetics of Water-Rock Interaction. Springer, 545 - 589.

Thompson, J.B., Jr., 1970. Geochemical reaction and open systems. Geochim. Cosmochim. Acta 34, 529-551.

Trevena, A.S., Nash, W.P., 1979. Chemistry and provenance of detrital plagioclase. Geology **7**, 475-478.

White, A.F., Brantley, S.L., 2003. The Effect of Time on the Weathering of Silicate Minerals: Why Do weathering Rates Differ in the Laboratory and Field? Chem. Geol. 202, 479-506.

White, S. P., Allis, R. G., Moore, J., Chidsey, T., Morgan, C., Gwynn, W., and Adams, M., 2005. Simulation of reactive transport of injected CO_2 on the Colorado Plateau, Utah, USA. Chem. Geol. 217, 387-405.

Wildgust, N., Gorecki, C. D., and Bremer, J. M., 2011. An overview of the IEA Greenhouse Gas R&D Programme regional geologic storage capacity studies. Energy Procedia 4, 4835-4840.

Xu, T., Apps, J.A., Pruess, K., 2003. Reactive geochemical transport simulation to study mineral trapping for CO_2 disposal in deep arenaceous formations. J. Geophys. Res. 108, 2071.

Xu, T., Apps, J.A., Pruess, K., 2004. Numerical simulation of CO_2 disposal by mineral trapping in deep aquifers. Appl. Geochem. 19, 917-936.

Xu, T., Apps, J.A., Pruess, K., 2005. Mineral sequestration of carbon dioxide in a sandstone-shale system. Chem. Geol. **217**: 295-318.
Xu, T., Apps, J.A., Preuss, K., Yamamoto, H., 2007. Numerical modeling of injection and mineral trapping of CO_2 with H_2S and SO_2 in a sandstone formation. Chem. Geol. 242, 319-346.

Table 1. Saline sandstone reservoir characteristics and extent of CO_2 sequestration from published models

Reference, model, and pertinent parameters (where available)[1]	Major brine chemistry[2] (molal)	Mineralogy[3,4] (volume fraction)	Notes
(Audigane et al., 2007) TOUGHREACT Sliepner, Norway T: 37°C P: 100 bar ø: 0.42 k: 3×10^{-12} m^2 t: 10,000 a	Na: 0.5439 K: 1.553×10^{-3} Ca: 3.701×10^{-4} Mg: 2.576×10^{-6} Cl: 0.5375 HCO_3: 1.973×10^{-2} SO_4: 1.024×10^{-15} SiO_2: 1.811×10^{-4} pH: 7.67	chalcedony: 0.769↑ K-feldspar: 0.069↑ calcite: 0.067↓ muscovite: 0.052↓↓ albite: 0.030↓ chlorite: 0.013↓ siderite: 0.0↑ kaolinite: 0.0↑ dolomite: 0.0↑ magnesite: 0.0↑ dawsonite: 0.0↑↑	~ 6% CO_2 trapped in minerals
(Johnson et al., 2001, 2004) NUFT Sliepner, Norway T: 37°C P: 90-110 bar ø: 0.35 k: 3×10^{-12} m^2 t: 20 a	Na: 0.452 K: 5.3×10^{-3} Ca: 7.43×10^{-3} Mg: 1.813×10^{-2} Cl: 0.5213 HCO_3: 2.32×10^{-3} SO_4: 0.0 SiO_2: 1.664×10^{-4} pH: 7.0–7.2	quartz: 0.80 K-feldspar: 0.10 oligioclase: 0.05 muscovite: 0.03 phlogopite: 0.02 calcite: 0.0 ↑ magnesite: 0.0 ↑ dawsonite: 0.0 ↑	< 1% CO_2 trapped in minerals
(Knauss et al., 2005) CRUNCH Frio Fm., TX, USA T: 64°C P: 100 bar ø: 0.30 k: $\times10^{-12}$ m^2 t: 100 a	Na: 1.7767 K: 1.0594×10^{-2} Ca: 5.5291×10^{-2} Mg: 1.9001×10^{-2} Cl: 1.9394 $CO_{2(aq)}$:1.0097×10^{-3} SO_4: 1.0746×10^{-4} SiO_2: 4.0135×10^{-4} pH: 6.74	quartz: 0.6006 K-feldspar: 0.0426 labradorite: 0.0248 illite: 0.0096 calcite: 0.0071 kaolinite: 0.0066 chlorite: 0.0051 pyrite: 0.0035 calcite: 0.0 ↑ magnesite: 0.0 ↑ dawsonite: 0.0 ↑	6.9 vol% carbonate minerals after 100 a Model also considered the addition of SO_2 and H_2S to CO_2
(Liu et al., 2011) TOUGHREACT Mt. Simon sandstone, IL, IN, KY, USA T: 75°C P: 200 bar	Na: 1.596 K: 3.108×10^{-2} Ca: 3.547×10^{-1} Mg: 1.033×10^{-1} Cl: 2.545 HCO_3: 1.724×10^{-3}	quartz: 0.6261 K-feldspar: 0.2120 ↓↓ dolomite: 0.0075 ↓ oligoclase: 0.0044 ↓ alunite: 0.0 ↑ anhydrite: 0.0 ↑	~2 vol% carbonate minerals at 10,000 a

Z: 2000 m ø: 0.15 k: 1×10^{-13} m^2 t: 10,000 a	SO_4: 1.408×10^{-2} SiO_2: 0.0 pH:6.9	calcite: 0.0 ↑ magnesite: 0.0 ↑ ankerite: 0.0 ↑ dawsonite: 0.0 ↑ smectite: 0.0 ↑ illite: 0.0 ↑	
(Gunter et al., 2000) PATHARC Glauconitic Sandstone Alberta Basin, Canada T: 54°C P: ~130 bar Z: 1480 m ø: 0.12 k: t: 1000 a	Na: 1.25 K: 1.77×10^{-2} Ca: 7.42×10^{-2} Mg: 2.38×10^{-2} Cl: 1.45 HCO_3: 3.25×10^{-3} SO_4: 3.81×10^{-3} SiO_2: 0.0 pH:7.2	quartz: 0.87 annite: 0.05 ↓ K-feldspar: 0.02 ↓ kaolinite: 0.02 ↓ albite: 0.01 ↓ calcite: 0.01 dolomite: 0.01 siderite: 0.01 ↑↑ illite: 0.0 ↑	Mineral trapping is the major trapping mechanism. Model also considered the addition of H_2SO_4 and H_2S to CO_2
(White et al., 2005) ChemTOUGH White Rim sandstone, UT, USA T: 54°C P: 100 bar Z: ø: 0.15 k: 2×10^{-13} m^2 t: 100,000 a	Na: 0.292 K: 2.7910^{-3} Ca: 8.2×10^{-2} Mg: 0.0 Cl: 0.293 HCO_3: 2×10^{-6} SO_4: 0.0 SiO_2: 2.4×10^{-2} pH: 11.7	quartz: 0.77 kaolinite: 0.0225 ↑ smectite: 0.0225 calcite: 0.018 ↑ anorthite: 0.0066 ↓ K-feldspar: 0.006 ↓ albite: 0.006 ↓ dawsonite: 0.0 ↑ siderite: 0.0 dolomite: 0.0 illite: 0.0	Reactions nearly complete after 10,000 yr ~13% of CO_2 trapped as calcite and dawsonite
(Xu et al., 2003, 2004) TOUGHREACT Gulf Coast Sediments (Frio Fm., TX, USA) T: 40°C P: 100 bar Z: ~ 1000 m ø: 0.10 k: 1×10^{-13} m^2 t: 10,000 a	Na: 1.047 K: 1.801×10^{-2} Ca: 3.470×10^{-3} Mg: 1.637×10^{-4} Cl: 1.061 HCO_3: 9.291×10^{-4} SO_4: 1.323×10^{-9} SiO_2: 1.147×10^{-4} pH: 7.7	quartz: 0.56 ↑ oligoclase: 0.20 ↓↓ K-feldspar: 0.08 ↓ smectite: 0.04 ↓ clinochlore: 0.03 ↓ kaolinite: 0.02 ↓ calcite: 0.02 ↑ daphnite: 0.02 ↓ illite: 0.01 ↑ hematite: 0.01 ↓ kerogen: 0.01 ↓ dawsonite: 0.0 ↑ ankerite: 0.0 ↑	~90 kg CO_2/m^3 trapped in carbonate minerals, mostly dawsonite and ankerite, after 10,000 a
(Xu et al., 2004) TOUGHREACT Alberta Basin, Canada T: 54°C (glauc. ss) P: 260 bar Z: 1500 m ø: 0.12 k: t: 10,000 a	Na: 1.0 K: 0.0 Ca: 0.0 Mg: 0.0 Cl: 0.0 HCO_3: 0.0 SO_4: 0.0 SiO_2: 0.0 pH: 7	quartz: 0.7128 glauconite: 0.044 ↓↓ illite: 0.0264 ↑ kerogen: 0.0264 K-feldspar: 0.0176 ↑ kaolinite: 0.0176 calcite: 0.0088 dolomite: 0.0088 ↑ siderite: 0.0088 ↑↑	~17 kg CO_2/m^3 trapped in carbonate minerals, mostly siderite and ankerite, after 10,000a

		oligoclase: 0.0088 dawsonite: 0.0 ↑ ankerite: 0.0 ↑↑	
(Xu et al., 2005) also see (Xu et al., 2007) TOUGHREACT Frio Fm., TX, USA T: 75°C P: 201 bar Z: 2 km ø: 0.30 k: 1×10^{-13} m^2 t: 100,000 a	Na: 0.99 K: 7.52×10^{-3} Ca: 3.23×10^{-3} Mg: 1.53×10^{-7} Cl: 1.0 HCO_3: 4.32×10^{-2} SO_4: 1.32×10^{-9} SiO_2: 7.26×10^{-4} pH: 7.34	quartz: 0.58 ↑ oligoclase: 0.198 ↓↓ K-feldspar: 0.082 ↓ chlorite: 0.0455 ↓↓ Na-smectite: 0.04 ↓ kaolinite: 0.0202 ↓ calcite: 0.0193 ↓ illite: 0.01 hematite: 0.005 albite: 0.0 ↑ siderite: 0.0 ↑ ankerite: 0.0 ↑↑ dawsonite: 0.0 ↑↑	~90 kg CO_2/m^3 trapped in carbonate minerals after 100,000 a Rock contains ~4 vol% ankerite and ~6 vol% dawsonite after 100,000 a
(Xu et al., 2005) TOUGHREACT Frio "C" Fm., TX, USA T: 59°C P: 152 bar Z: 1541–1546 m ø: 0.34 k: 2.3 x 10^{-12} m^2 t: 1,000 a	Na: 1.35 K: 4.53×10^{-3} Ca: 6.6×10^{-2} Mg: 2.2×10^{-2} Cl: 1.49 C: 5.04×10^{-2} S: 4.20×10^{-5} SiO_2: 2.50×10^{-4} pH: 6.7	quartz: 0.579 oligoclase: 0.198 K-feldspar: 0.082 chlorite: 0.0456 Na-smectite: 0.039 kaolinite: 0.020 calcite: 0.019 ↓ illite: 0.0095 ↑ hematite: 0.005 albite: 0.0 siderite: 0.0 ↑↓ ankerite: 0.0 ↑ dawsonite: 0.0 ↑	~ 9kg CO_2/m^3 trapped in carbonate minerals after 1,000 a Rock contains ~1 vol% ankerite after 1,000 a

[1] T = temperature, P = pressure, Z = depth, ø = porosity, k = permeability, and t = time.
[2] The brine chemistry column lists only the species most abundant in natural waters for simplicity. Refer to original papers for additional species in the published models.
[3] The mineralogy fraction is reported in the manner of the individual paper (note that some mineralogies are normalized to account for porosity and some are not).
[4] Change in mineral abundance during model evolution: ↑↑ for large increase, ↑ for moderate increase, ↓ for moderate decrease, ↓↓ for large decrease.

Table 2. Baseline sandstone mineralogy

Mineral	Composition	Mass %	Vol.%, (100 Φ_m)	Size (mm)	SSA_{geom} [1] (m^2/g)	n^g [2] (m^{-3})
Quartz	SiO_2	65	48.75	1.00	$2.3x10^{-3}$	$4.9\ x10^{8}$
Microcline	$KAlSi_3O_8$	18	13.50	0.125	$1.9x10^{-2}$	$6.9\ x10^{10}$
Oligoclase	$Ca_{0.2}Na_{0.8}Al_{1.2}Si_{2.8}O_8$	8	6.00	0.125	$1.8x10^{-2}$	$3.1\ x10^{10}$
Calcite	$CaCO_3$	5	3.75	0.500	$4.4x10^{-3}$	$3x10^{8}$
Smectite	$K_{0.03}Ca_{0.39}Al_{1.77}Si_{3.97}O_{10}(OH)_2$	3	2.25	0.001	$2.27x10^{0}$	$2.3\ x10^{16}$
Illite	$KAl_3Si_3O_{10}(OH)_2$	1	0.75	0.001	$2.12x10^{0}$	$7.5\ x10^{15}$
Porosity	--		25.00		---	

[1] Geometric specific surface area
[2] Number of mineral grains per unit volume of a porous medium

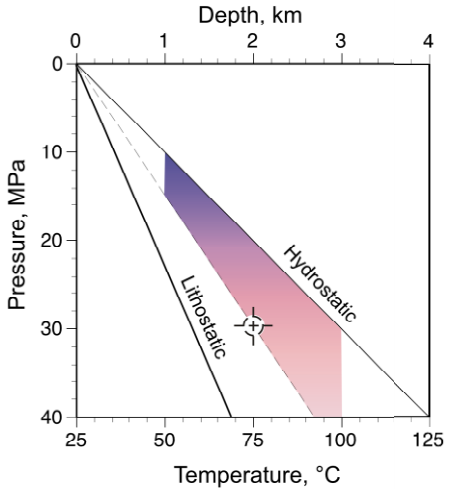

Figure 1. The shaded field shows the ranges of temperature and CO_2 pressure that are likely to occur in a CO_2 storage reservoir. The circular, crossed symbol shows the temperature (75°C) and CO_2 pressure (30 MPa) chosen for the baseline model.

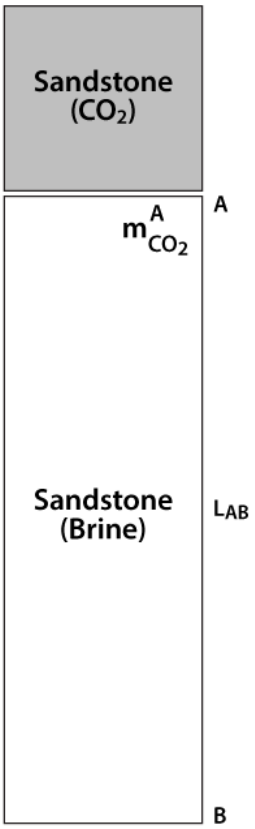

Figure 2. Schematic diagram of the one-dimensional reactive diffusion model. Upon initiation of the simulation, the sandstone contains a brine of composition shown in Table 3. *A* represents the interface between the CO_2 SC fluid and the brine, and is impermeable to salt. *B* represents the no-flow boundary. Models were run as described in text with different values for the distance between A and B (L_{AB}). The system diagrammed here is a small piece of the entire plume-rock system as shown in Figure 3.

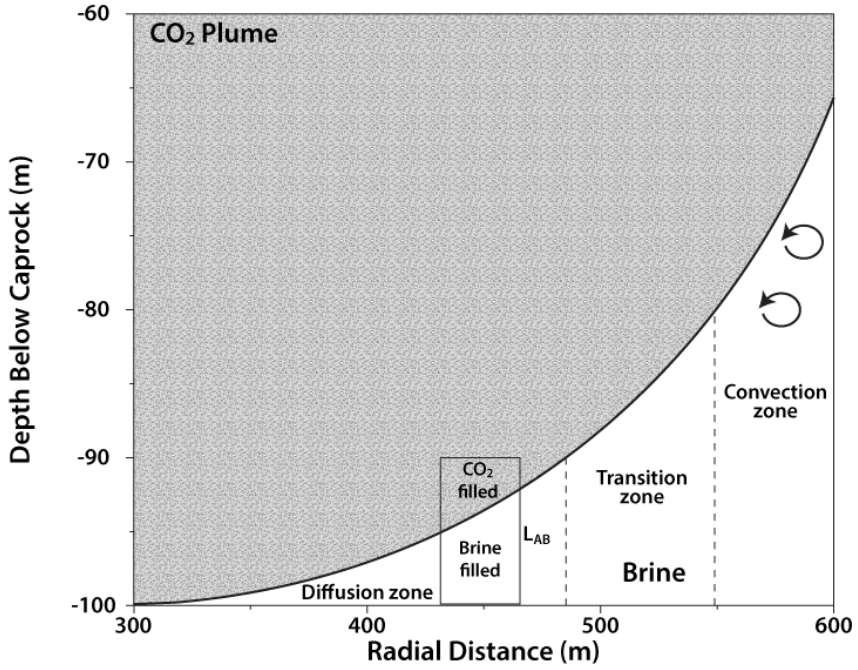

Figure 3. A schematic diagram of relative depth showing schematic geometry of a CO_2 plume within a sandstone sandwiched between two shales. The overlying shale caprock is located at a depth of 0 in the diagram; the lower-lying shale lies at a depth of -100 m. The interface between the plume (grey) and the brine (white) within the sandstone forms a curved interface, as shown, relatively soon after injection. The rectangular box is the system of study, expanded in Figure 2: L_{AB} is the distance from the underlying shale (depth = -100 m) to the CO_2 plume-brine interface. Figure redrawn following Fig. 5.7 in Benson and Cook (2005).

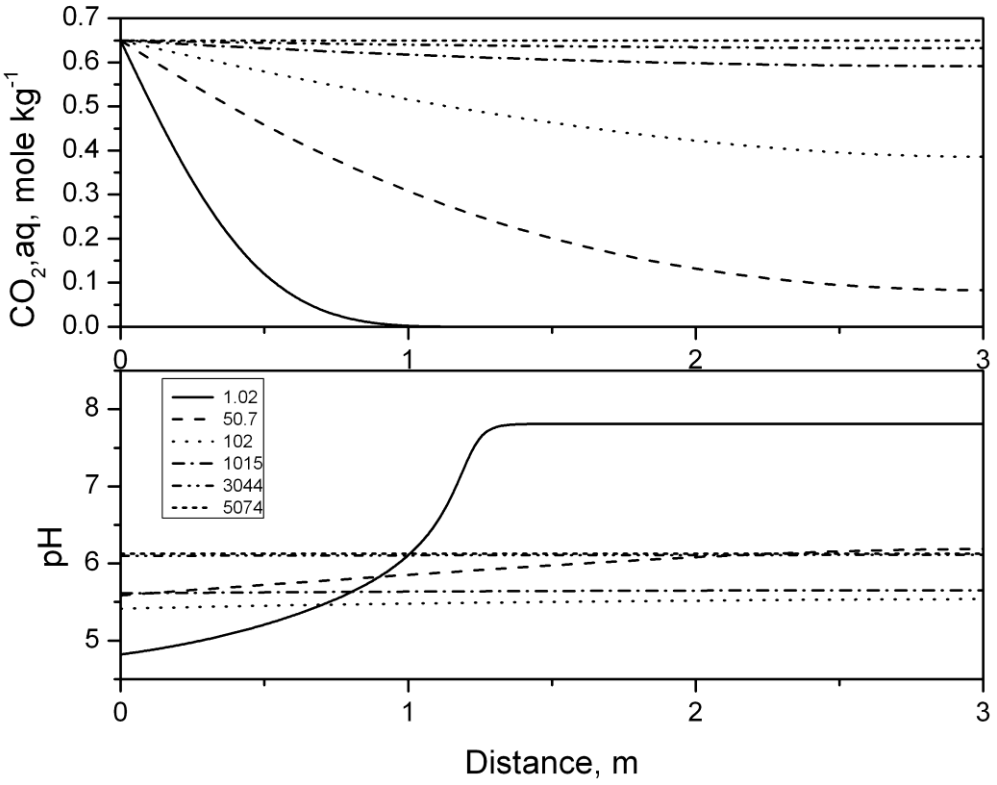

Figure 4. The calculated concentrations of $CO_{2,aq}$ (top) and pH (bottom) plotted as a function of distance inside the sandstone layer at different times (years) as noted for the reactive diffusion model with L_{AB} = 3m. Note that here, distance is the distance downward away from the buoyant CO_2 plume, toward the lower shale caprock (compare with Figures 2 and 3.

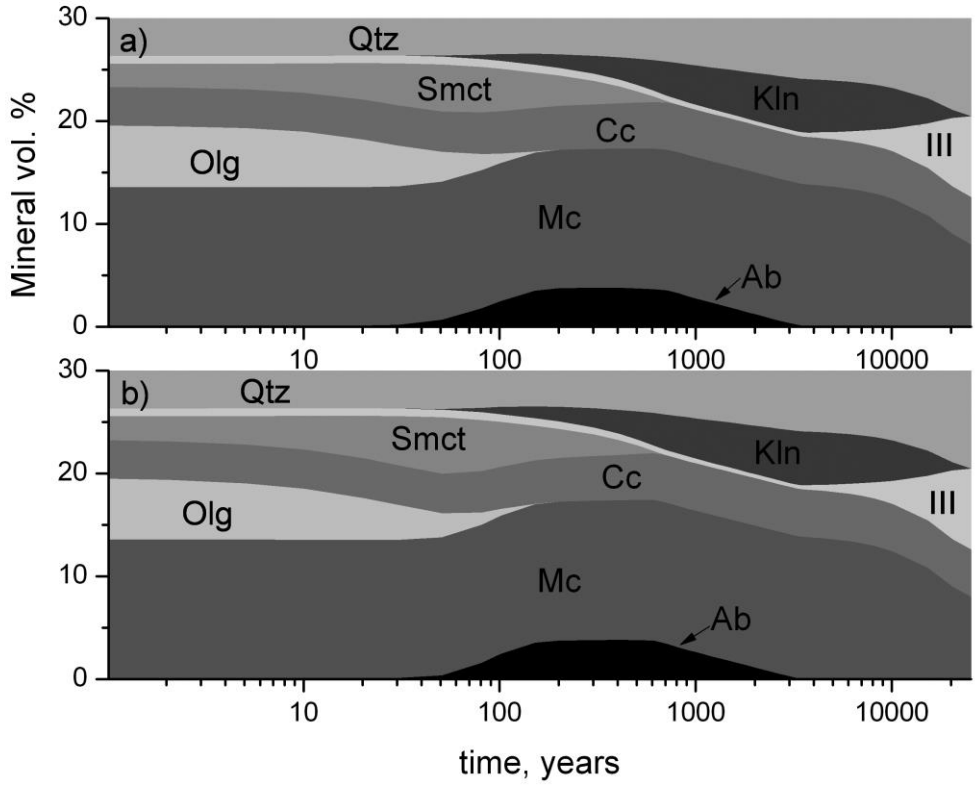

Figure 5. The calculated mineral composition plotted versus time for a) L_{AB} = 3 m, b) L_{AB} = 1 m. The composition was averaged across the entire layer of sandstone (i.e. across L_{AB} in Fig. 2). The figure documents that mineral evolution is the same for two small values of L_{AB}, i.e., as long as $L_{AB} < L^{*}_{AB}$ where this latter value is about 20 m (see text).

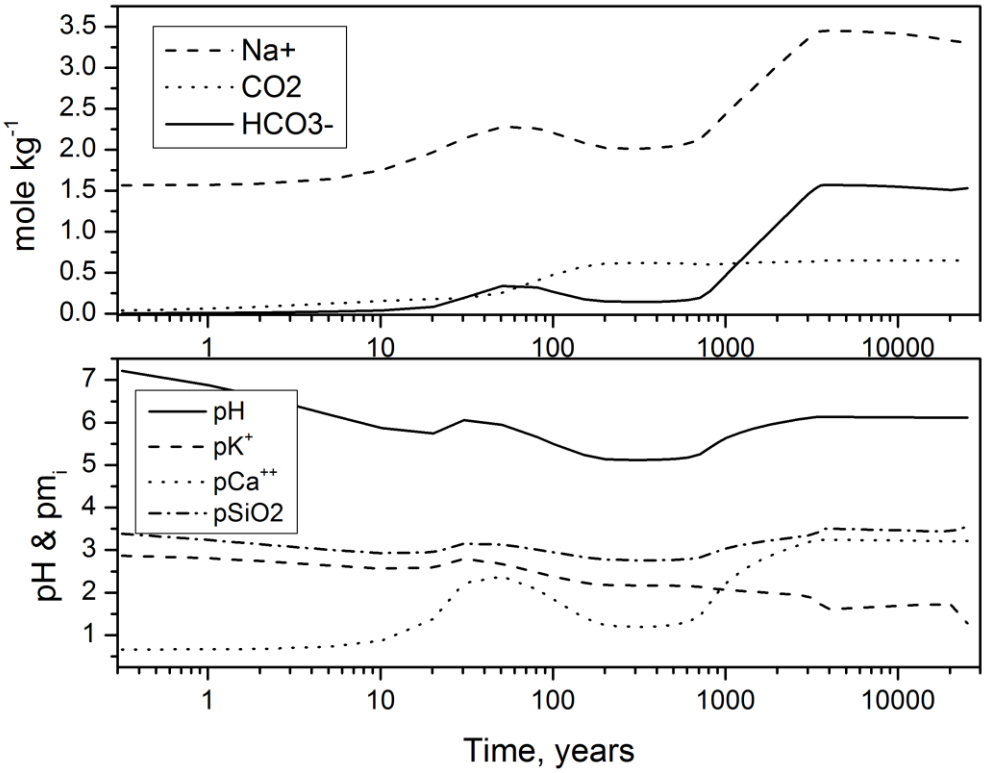
Na+
CO2
HCO3-
mole kg-1
pH
pK+
pCa++
pSiO2
pH & pmi
Time, years

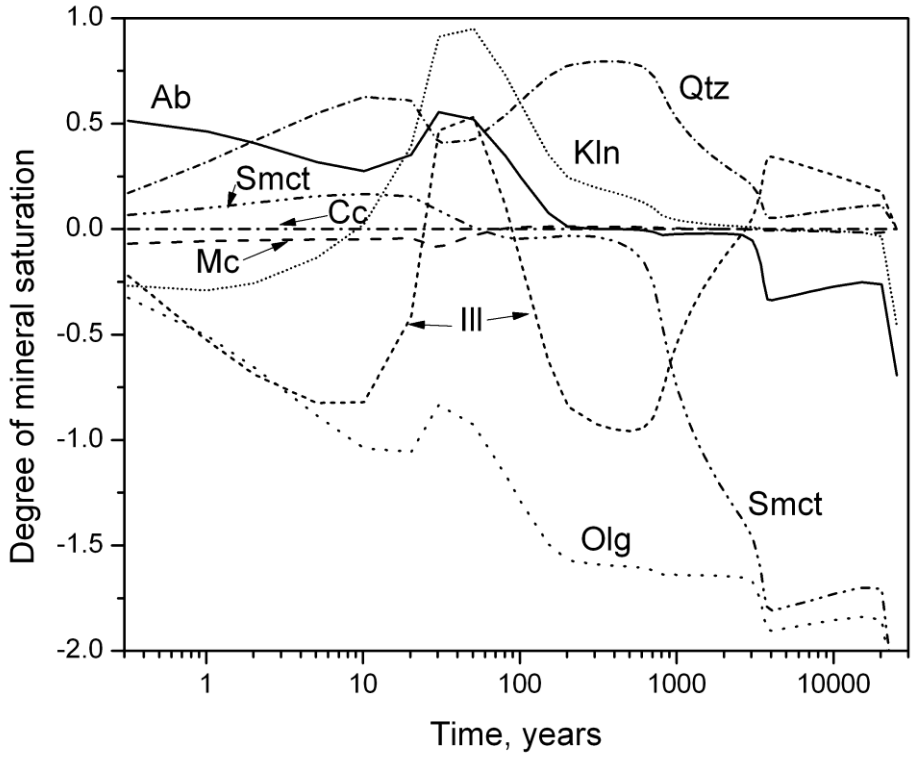
Ab
Qtz
Kln
Smct
Cc
Mc
Ill
Smct
Olg
Degree of mineral saturation
Time, years

Figure 6. Top graph: plot of average molalities of Na^+, $CO_{2(aq)}$ and HCO_3^- versus time. Middle graph: plot of average pH and -log $m_{i,aq}$ versus time. Here "pm_i" refers to $-\log(m_i)$. All simulations for L_{AB} = 3 m. Bottom graph: average saturation indices, log (Q/K_{eq}), for minerals plotted versus time for the sandstone model with L_{AB} = 3 m.

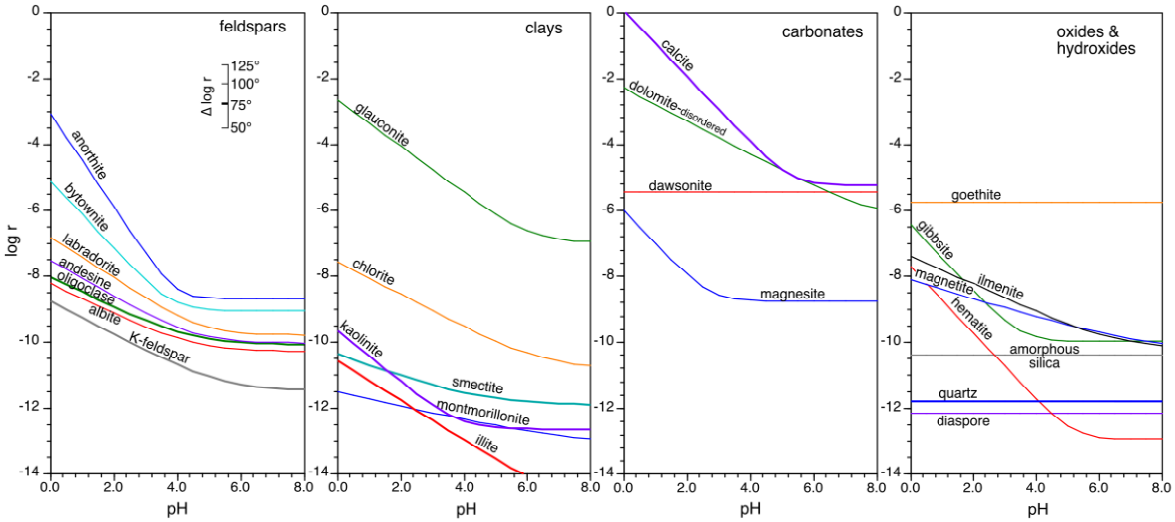

Figure 7. Comparison of the mineral dissolution rates at 75°C (Marini, 2007) that may be important in rocks of a deep saline CO_2 storage reservoir. The dissolution rates of minerals considered in the baseline model are plotted using heavier lines.

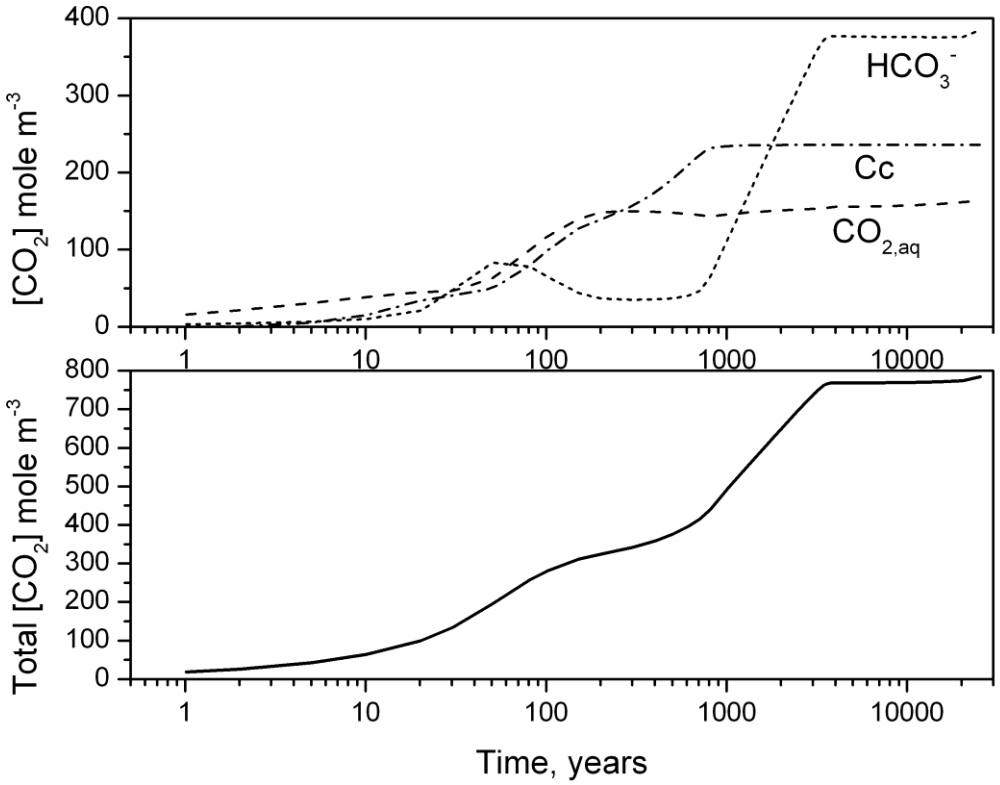

Figure 8. The average CO_2 stored per m^3 of a sandstone layer of 3m thickness. Top: the dashed line shows the direct CO_2 dissolution in aqueous brine by plotting the concentration of $CO_{2(aq)}$; the short-dashed line corresponds to CO_2 dissolution with

conversion into HCO_3^-; the dot-dashed line corresponds to mineral trapping due to calcite precipitation. Bottom: the total sum of stored CO_2 by the three mechanisms. The maximum stored CO_2 equals 784 mole per m^3 sandstone, or 34.5 kg CO_2 per m^3.

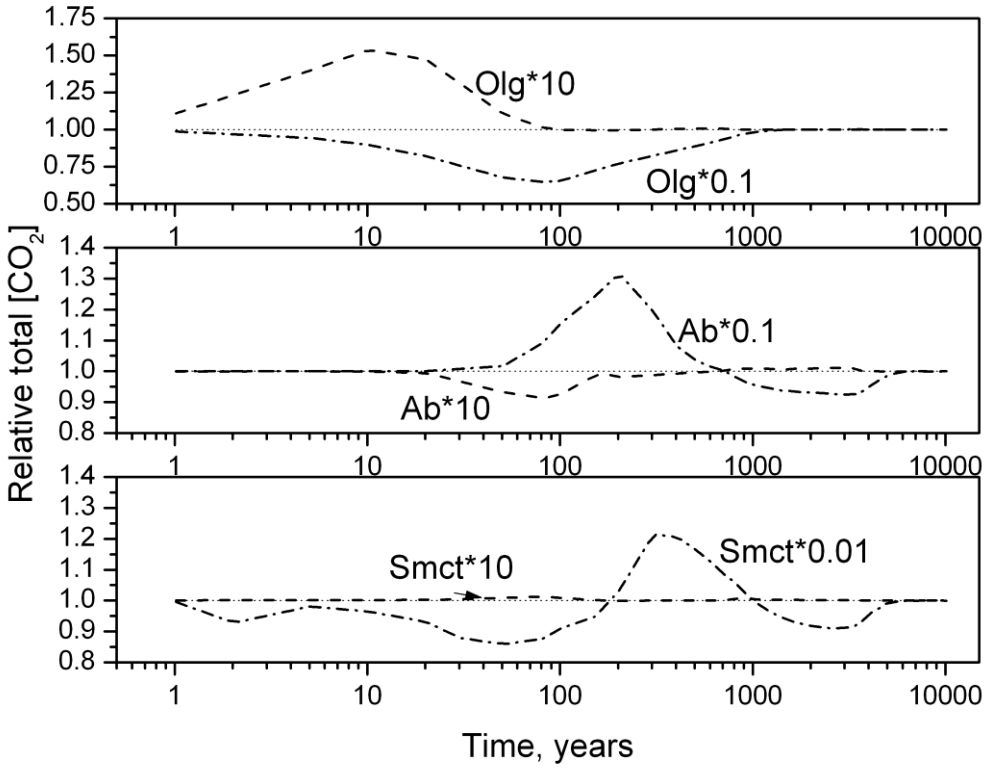

Figure 9. The effect of changes in the rate constants for oligoclase, albite and smectite on the relative total CO_2 stored in the sandstone (*sensitivity factor*, $[CO_2]^{var} / [CO_2]^{std}$, see details in text) plotted versus time. In the Ab and Smct cases, the sequestration is most sensitive to a decrease in the rate constants rather than an increase. This is because a decrease moves the system into the regime of kinetic limitation whereas an increase causes the system to approach equilibrium. Note that the ordinate is scaled differently in the panels; for example, in this figure, the sensitivity factor for changing the oligoclase rate constant is the largest.

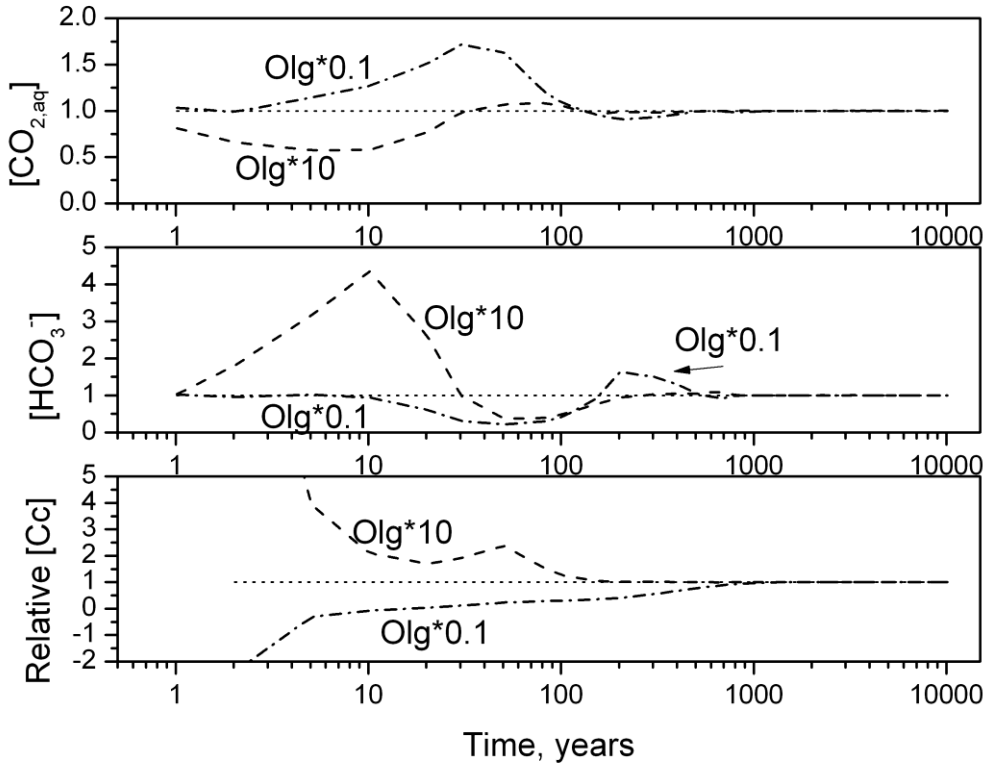

Figure 10. The effect of the oligoclase rate constant on CO_2 sequestration for the three mechanisms. The sequestration is most sensitive to a 10x decrease in the rate constant after about 10 a.

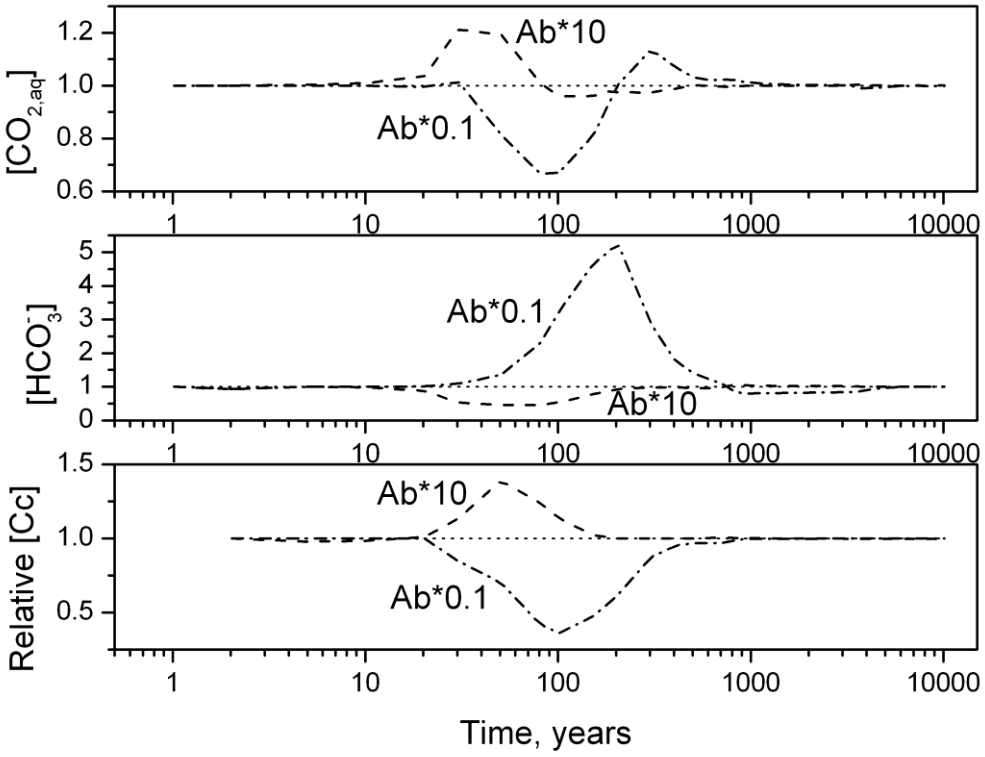

Figure 11. The effect of changes in the albite rate constant on CO_2 storage over time by the three different mechanisms. Storage is more sensitive to a 10x decrease in the rate constant than an increase, starting from about 20 a on.

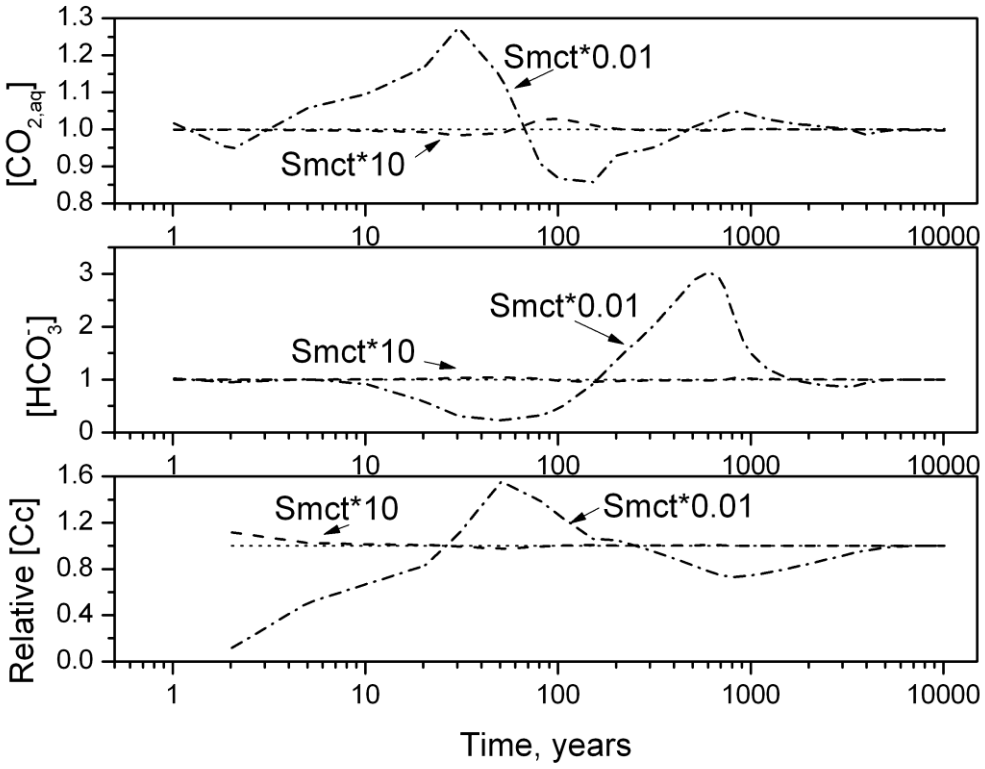

Figure 12. The effect of changes in the smectite rate constant on CO_2 stored versus time for the three sequestration mechanisms. Storage is sensitive to a 100x decrease in the rate constant starting at 10 a.

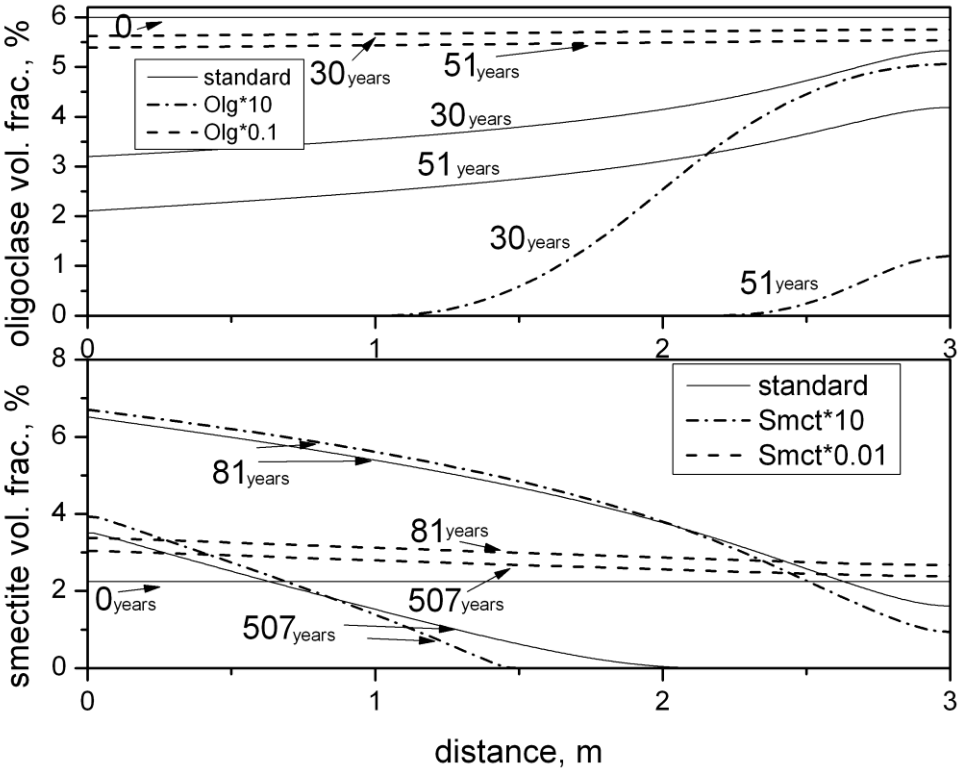

Figure 13. Plots of oligoclase (top) and smectite (bottom) volume fractions versus distance inside the 3 m-thick sandstone layer for different values of the oligoclase and smectite kinetic constant. The numbers mark the profile times in years.

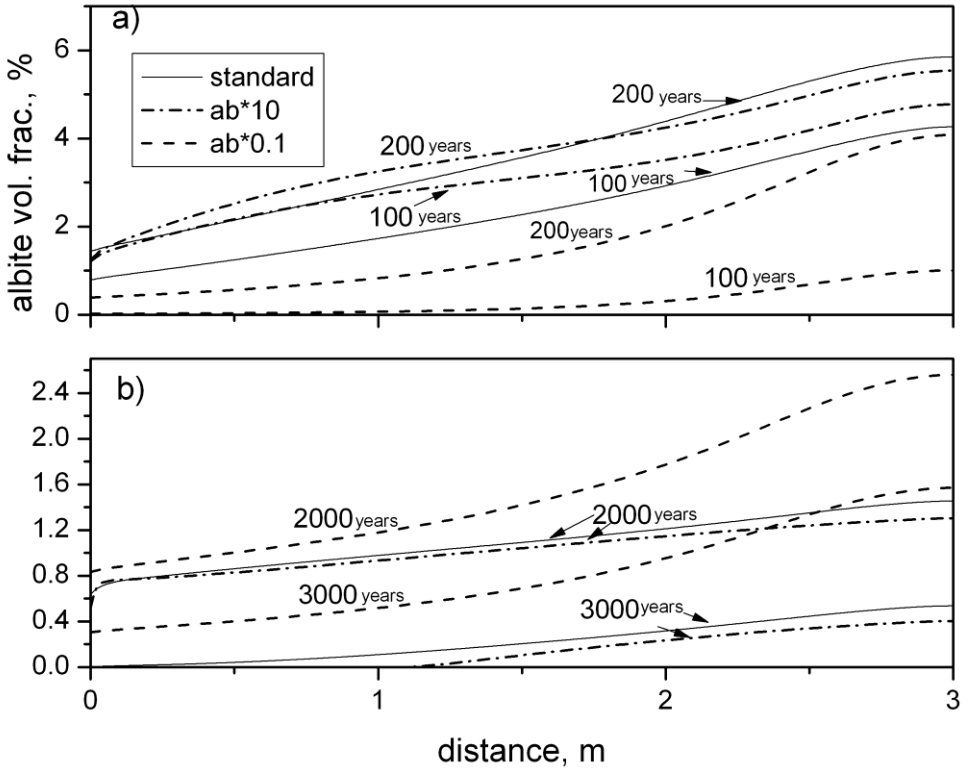

Figure 14. Plots of albite volume fractions versus distance inside the 3 m-thick sandstone layer plotted for different values of the albite kinetic constant. The numbers mark the profile times in years: a) albite precipitation waves; b) albite dissolution waves. Note that distance plotted horizontally on this figure corresponds to depth downward from interface A in Figure 2.

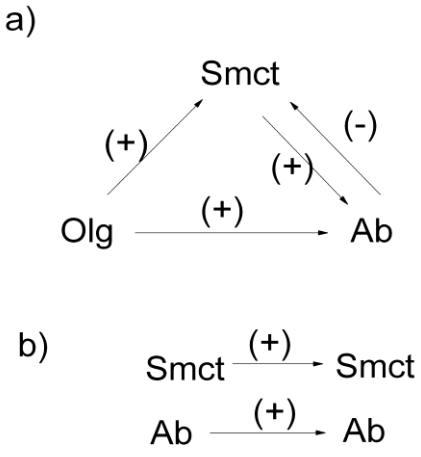

Figure 15. Interaction among minerals during CO_2 sequestration. The arrows show the direction of kinetic coupling, where (+) corresponds to positive kinetic coupling and (-) refers to negative kinetic coupling. a) The coupling between different minerals; b) a positive auto-response to smectite and albite kinetic constants is also observed.

Table 3. Baseline brine composition[1] based on average oil-field brine compositions

	Average brine (molality) [2]	Theoretical brine (molality)[3]
pH	-	7.81
Cl^-	2.146	2.146
Na^+	1.620	1.712
Ca^{2+}	0.258	0.217
K^+	0.012	1.1×10^{-3}
Al^{3+}	-	9.9×10^{-8}
SiO_2	-	3.0×10^{-4}
HCO_3^-	0.0040	9.5×10^{-5}

[1] The molalities are given as component molalities, i.e, as the sum over all species containing the component.
[2] Composition is based on North American oil-field brines as summarized in the Supp Material, Table S1, where data were from (Collins, 1975).
[3]This column shows the initial composition of aqueous brine in equilibrium with the mineral assemblage Qtz+Mc+Ill+Cc+Olg+Smct. The ionic strength of this solution is 2.41. This is the brine composition used for the baseline model.

Table 4. Dissolution rate parameters for minerals

Mineral	Acidic Mechanism			Neutral Mechanism				Basic Mechanism		
	E_H kJ mol^{-1}	A_H mol $m^{-2}s^{-1}$	n_H	E_W kJ mol^{-1}	A_W mol $m^{-2}s^{-1}$	E_{OH} kJ mol^{-1}	A_{OH} mol $m^{-2}s^{-1}$	n_{OH}	b_H	b_{OH}
Quartz	-	-	-	87.6	22.91	108.37	10	-0.5	1	0
Albite	65	33.11	0.457	69.8	1.55	71	$2.88\ 10^{-5}$	-0.572	1	0
Microcline	51.7	0.1	0.5	38	$1.78\ 10^{-6}$	94.1	$1.95\ 10^{-5}$	-0.823	1	0
Oligoclase	65	52.48	0.457	69.8	2.45	-	-	-	1	0
Calcite	14.4	165.96	1	23.5	0.02	35.4	524.81	1	1	0
Smectite	23.6	1.41	0.34	35	$2.24\ 10^{-7}$	58.9	$6.31\ 10^{-7}$	-0.4	1	0
Illite[1]	46	$2.2\ 10^{-4}$	0.6	14	$2.5\ 10^{-13}$	67	0.27	0.6	0	1
Kaolinite	65.9	1.74	0.777	22.2	$5.13\ 10^{-10}$	17.9	$1.23\ 10^{-14}$	-0.472	1	0

[1]Köhler et al. (2003). All data otherwise from Palandri and Kharaka (2004).

Table 5. Summary of mineral/ fluid reactions[1] due to CO_2 invasion into sandstone.

Reaction Progress	**0 – 10 a**	**10 – 50 a**	**50 – 100 a**	**100-1,000 a**	**1,000 – 5,000 a**	**5,000 – 10,000 a**
< 0.1	Mc↓ Cc ↑	Mc↓ Ab ↑	Mc↓ Kln ↑	Mc↑ Ab ↑	Mc↑	
0.1 – 0.9	Olg ↓	Smct ↑ Olg ↓ Cc ↑	Ab ↑ Smct ↓ Olg ↓	Kln ↑ Smct ↓	Kln ↑ Ab ↓	Ill ↑ Kln ↓ Mc ↓
> 0.9	Smct ↑		Cc ↑	Cc↑		

[1]The symbols M ↓ and M ↑ correspond to mineral dissolution and precipitation, respectively.